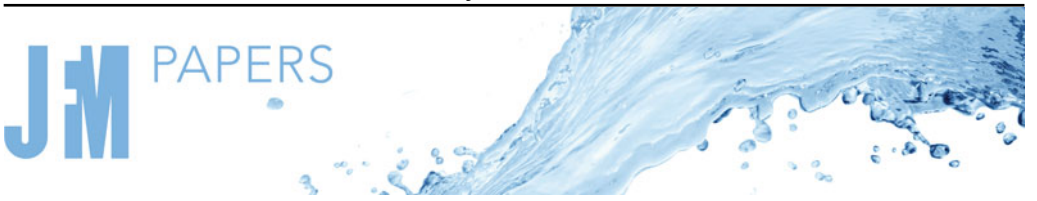
J. Fluid Mech. (2026), *vol.* 1038, A19, doi:10.1017/jfm.2026.11751



Mach reflection of a detonation wave over a concave double wedge

Zhen-Yang Zhou[1], **Hong-Hao Ma**[1] **and Lu-Qing Wang**[1]

[1]Department of Modern Mechanics, University of Science and Technology of China, Hefei, Anhui 230026, PR China

Corresponding author: Lu-Qing Wang, aiyuan@ustc.edu.cn

(Received 6 February 2026 UTC; revised 22 April 2026 UTC; accepted 1 June 2026 UTC)

In this study, the Mach reflection of a detonation wave in $2H_2 + O_2 + 2Ar$ over a concave double wedge was experimentally investigated. Three Mach reflection configurations could be observed successively, namely, Mach reflection of a Chapman–Jouguet detonation over the first surface, Mach reflection of an overdriven detonation wave over the second surface, and Mach reflection after the interaction of two triple points. The experimental results indicated that the classical reactive theories based on the straight Mach stem assumption are unable to accurately predict the behaviours of the latter two Mach reflections. The asymptotic triple-point trajectory angle of the secondary Mach reflection, χ_2, is significantly smaller than the theoretical prediction. A curved model for the Mach stem m_1 is constructed, introducing a curved Mach stem near the triple point. The Mach stem has a concave curvature, implying a lower overdrive degree and a smaller incident angle, which consequently leads to a reduction in χ_2. Based on the curved Mach stem model, an equivalent wedge angle Φ and an equivalent overdrive degree $\overline{\alpha}$ are introduced to predict the value of χ_2. An analytical model for solving the interaction of two triple points was developed. Two different wave structures after the interaction – namely, downward-travelling shock–shock and downward-travelling centred shock–expansion – were determined using gas dynamic and shock dynamic methods. The curved Mach stem m_1 can result in the variation of the wave structure.

Key words: detonation waves

1. Introduction

The interaction between a detonation wave and a wedge is important considering its application in propulsion systems (Wolański 2013). Detonation reflections over complex geometries – such as double wedges – are important for the design of pulse detonation engines and rotating detonation engines. Regular reflection (RR) or Mach reflection (MR) occurs when a planar detonation wave collides with a wedge (Ong 1955; Akbar 1971).

© The Author(s), 2026. Published by Cambridge University Press.

https://doi.org/10.1017/jfm.2026.11751 Published online by Cambridge University Press

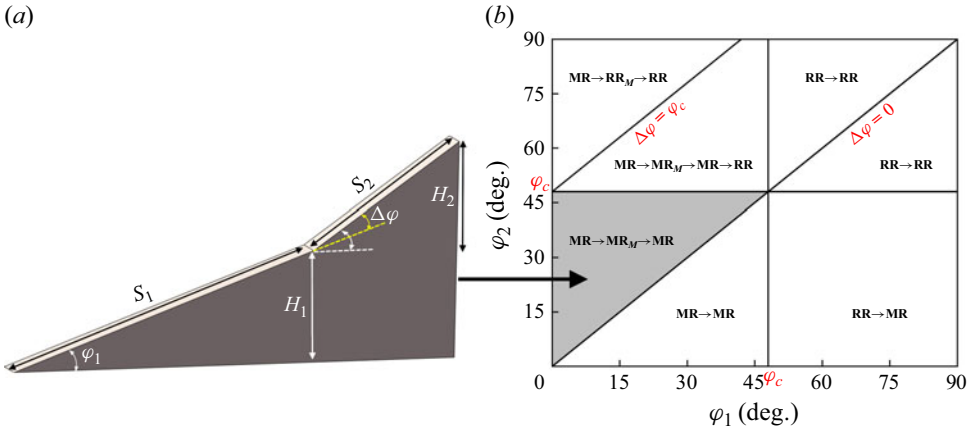


Figure 1. Sketch of a double-wedge reflector and regions of reflection processes over a double-wedge surface. Here, S_1 is the length of the first surface, S_2 is the length of the second surface, φ_1 is the angle of the first wedge, φ_2 is the angle of the second wedge, and $\Delta\varphi = \varphi_2 - \varphi_1$.

The RR configuration consists of the incident wave i and the reflected wave r, which can be observed when the wedge angle (φ) exceeds the MR-RR transition angle (φ_c). The MR process can be analysed in the following way. When the incident detonation wave passes over the compressive corner, the gas flow induced by the moving detonation is disturbed. As a result, a family of cylindrical compression waves is generated at the leading edge of the wedge. These compression waves propagate with the local sound speed relative to the local flow velocity, and coalesce forming a shock–shock (or a detonation–detonation as named by Li & Ben-Dor 1998) that intersects with the incident detonation. Consequently, a triple point T forms, associated with an incident detonation i, a reflected shock r, a straight Mach stem m, and a slipstream s. When a plane detonation wave encounters a double wedge (figure 1*a*), different types of reflection processes can be observed, depending on the wedge angles. Ben-Dor, Dewey & Takayama (1987), Ben-Dor *et al.* (1988) and Takayama & Ben-Dor (1988) have studied the reflection of a planar shock wave over a double wedge both analytically and experimentally. In their analytical study, seven inert shock wave reflection processes (figure 1*b*) could be determined. For the scenario concerned in this study (the grey region in figure 1*b*), three MRs occur successively. Figure 2 shows a hypothetical MR process of a detonation wave over a concave double wedge. Over the first surface, a classical MR phenomenon is indisputable (MR1). As the Mach stem m_1 encounters the second wedge, a secondary MR configuration (m_1 serves as the incident wave) is expected (MR2). After the interaction of the two triple points (T_1 and T_2), a tertiary MR associated with the original detonation wave i can be formed (MR3). There are currently no reported studies on the specific characteristics of these three MRs of detonations over a concave double wedge. Only a numerical study conducted by Li *et al.* (2022) reported seven reflection processes of detonation reflections over concave and convex double wedges. However, the specific characteristics of reflection processes were not investigated in their study.

The primary MR over the first surface (MR1) is a classical pseudo-steady MR. Up to now, numerous investigations have been devoted to exploring the MR characteristics of gaseous detonations over a plane wedge (Edwards, Walker & Nettleton 1984; Meltzer *et al.* 1993; Li, Ben-Dor & Gronig 1997; Shepherd, Schultz & Akbar 1999; Thomas & Williams 2002; Fortin, Liu & Lee 2015; Li *et al.* 2018; Chen, Ma & Wang 2023; Zhou, Ma & Wang 2024). Due to the intrinsic thickness of the wave front, the detonation MR

https://doi.org/10.1017/jfm.2026.11751 Published online by Cambridge University Press

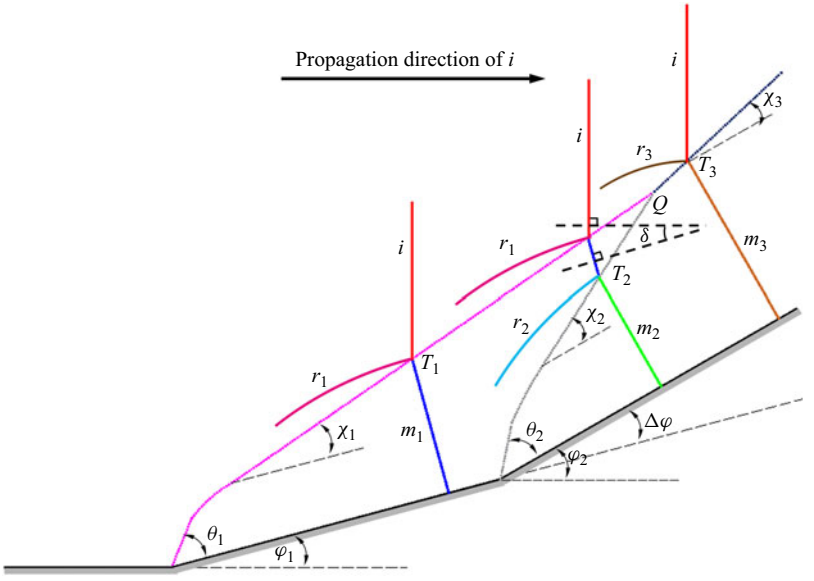


Figure 2. Sketch of the MR process over a concave double wedge. The MR structures evolve at different time instants. As the incident detonation wave propagates, three MR structures appear in sequence. Here, i is the incident wave, r is the reflection wave, m is the Mach stem, T is the triple point of the MR, φ is the wedge angle, θ is the triple-point trajectory angle in the frozen limit, χ is the triple-point trajectory angle in the equilibrium limit, Q is the collision point of two triple points, and δ is the deflection angle of the detonation surface.

process exhibits localised self-similarity. Near the leading edge of the wedge, the triple-point trajectory is consistent with that of an inert shock (frozen limit). In the far field, the self-similarity can be recovered asymptotically, which is called the 'equilibrium limit'. Li, Ning & Lee (2015) and Li & Lee (2016) confirmed the localised self-similarity of MR of Zeldovich-von Neumann-Döring (ZND) detonations and cellular detonations by numerical simulations. Fortin *et al.* (2015) and Li *et al.* (2018) experimentally confirmed the local self-similar triple-point trajectories of detonation MRs in various mixtures. Zhou *et al.* (2024) indicated the significant influence of velocity deficits on the self-similarity of MR. As illustrated in figure 2, the triple-point trajectory angle decreases from θ (near field) to χ (far field). Assuming that the Mach stem is straight, the two angles can be calculated using the non-reactive theories (Whitham 1957; von Neumann 1963) and the modified theories (Li *et al.* 1997; Li & Ben-Dor 1998), respectively. However, Li *et al.* (2018) indicated that with a large wedge angle (more than 30°), the final asymptotic triple-point trajectory angle is not in agreement with the theoretical results.

The secondary MR over the second surface (MR2) is an MR of an overdriven detonation wave. The Mach stem m_1, which is essentially an overdriven detonation wave, serves as the incident wave in MR2 (see figure 2). The modified theories indicate that the triple-point trajectory angle is very sensitive to the overdrive degree of the incident wave: $\alpha_i = M_i/M_{CJ}$, where M_i and M_{CJ} are the Mach numbers of the incident wave and the Chapman–Jouguet (CJ) detonation wave, respectively (Li *et al.* 1997; Li & Ben-Dor 1998). Steady decelerated detonation waves ($\alpha_i < 1$) can be achieved via porous media (Guo *et al.* 2002; Mazaheri *et al.* 2015; Sow, Semenko & Kasimov 2017; Zhou *et al.* 2024). Recently, the effects of velocity deficit on the MR process of a detonation wave were studied by Zhou *et al.* (2024). Overdriven detonations can be obtained in some fundamental detonation problems, such as flame acceleration and deflagration to detonation transition (Huang & Xu 1987; Guo *et al.* 2007), diffraction and re-initiation (Wang, Xu & Guo

https://doi.org/10.1017/jfm.2026.11751 Published online by Cambridge University Press

2008; Gray *et al.* 2017), critical diameter (Lee 1984; Desbordes 1988), and transition in different reactive mixtures (Li *et al.* 2008; Tang Yuk *et al.* 2018). Unfortunately, these overdriven detonations are unstable and temporary, which degrades into the normal state in a short distance. Thus there are hardly any reports of MR of overdriven detonation waves. Essentially, the Mach stem in the MR process is an overdriven detonation wave (Gavrilenko *et al.* 1979, 1983), which is relatively stable in the equilibrium limit (Ren, Jing & Li 2021). In addition, the height of the Mach stem and the triple-point trajectory over a plane wedge are predictable. Thus the Mach stem can serve as an ideal incident wave to study the MR of an overdriven detonation wave. However, the Mach stem was found to be curved near the triple point (Shepherd *et al.* 1999; Ohyagi *et al.* 2000; Fortin *et al.* 2015; Li *et al.* 2018). The influence of the curved Mach stem m_1 on the secondary MR remains unclear. Meanwhile, although the existence of the curved Mach stem has been proved by numerous experimental studies, none of them provides detailed descriptions and systematic analyses for this phenomenon.

The tertiary MR (MR3) takes place after the interaction of two triple points (see figure 2). For an inert incident shock wave, numerous investigations have been conducted. Ben-Dor *et al.* (1987, 1988) verified that for an inert incident shock wave, the tertiary MR approaches asymptotically the MR over a single wedge. Li & Ben-Dor (1999) studied the interaction of the two individual MRs in the concave double wedge problem by using von Neumann's three-shock theory. It was shown that the flow pattern behind the shock front is so complicated that additional assumptions are needed to give an analytical solution. Xie, Han & Takayama (2005) studied the wave structure after the interaction using a shock dynamic approach. In their study, a downward-travelling shock–shock disturbance on the Mach stem was predicted theoretically. However, for an incident detonation wave with chemical reactions, the wave structure after the interaction of two triple points can be different.

In this study, the MR of a detonation wave propagating in a $2H_2 + O_2 + 2Ar$ mixture over a concave double wedge was experimentally investigated using the soot foil technique. Then this paper attempts to analyse this problem using the methods of shock dynamics and gas dynamics. The remainder of this paper is organised as follows. Section 2 provides a theoretical model for MR of detonation waves. Section 3 describes the experimental set-up and provides the details of concave wedges. Next, the characteristics of the MR over the first surface, and the relation between the cell size and the overdrive degree, are discussed in § 4.1. In § 4.2, the characteristics of the MR of an overdriven detonation wave are presented, and a curved Mach stem model is established. In § 4.3, the processes of the MR after the interaction of two triple points are analysed using the gas dynamic method and the shock dynamic method. Finally, conclusions are presented in § 5.

2. Theoretical model for MR of detonation waves

The cellular detonation wave possesses a complex three-dimensional structure (Lee 1984), for which there is no suitable theoretical model. If one ignores this structure, then the detonation wave can be regarded as a reaction zone in which a fast exothermic chemical reaction occurs, led by a non-reactive shock wave. Unlike shock waves, the thickness of detonation waves is non-negligible for MR processes, presenting two limits (Fortin *et al.* 2015; Li *et al.* 2018; Zhou *et al.* 2024). In the near field (frozen limit), MR of detonation waves can be regarded as that of non-reactive shock waves, for which the non-reactive theories (Whitham 1957; von Neumann 1963) are suitable. In the far field (equilibrium limit), a simplified model – single-front model (Bartlmä 1990) and 2γ model (Li *et al.* 1997) – is adopted in this study. For the simplified model, the leading shock wave and the reaction zone are considered as a single discontinuity. Two specific heat ratios γ are used

https://doi.org/10.1017/jfm.2026.11751 Published online by Cambridge University Press

for the flow fields upstream (γ_0) and downstream (γ_1) of the discontinuity, respectively. The validity of the simplified model has been proved by the experimental investigation conducted by Li *et al.* (2018). With the simplified model of detonation waves, the process of MR in the equilibrium limit can be predicted by the modified three-shock (3S) theory (Li *et al.* 1997) and Chester–Chisnell–Whitham (CCW) theory (Li & Ben-Dor 1998), which are called reactive theories in this work. Note that the assumption of a straight Mach stem perpendicular to the wedge surface is necessary for these two theories.

The modified 3S theory (Li *et al.* 1997) is based on the oblique detonation wave relations, and this theory is called reactive 3S theory in this work. As M_{CJ}, γ_0, γ_1 are known for a certain mixture, the Mach number of the Mach stem (M_m) can be expressed as

$$M_m = F_{3S}(M_i, \varphi). \tag{2.1}$$

The analytical form of F_{3S} can be rather complicated (see details in Appendix A). Generally, once the Mach number of the incident wave (M_i) and the corresponding wedge angle (φ) are determined, M_m can be calculated by either oblique detonation wave relations (Li *et al.* 1997) or detonation polar (Bdzil & Short 2017).

The CCW theory, originally proposed by Whitham (1957), neglects the complex flows and waves behind the shock front. This method was later extended to the study of detonation waves (Li & Ben-Dor 1998), which is called reactive CCW theory in this work. In this framework, the triple point is regarded as a shock–shock (or detonation–detonation), which represents a discontinuity propagating on the detonation wave. The shock–shock relation can be written as

$$\tan\delta = \left(\frac{M_w}{M_u}\right)\left[1-\left(\frac{M_u}{M_w}\right)^2\right]^{\frac{1}{2}}\left\{1-\left[\frac{f(M_w)}{f(M_u)}\right]^2\right\}^{1/2}\left[1+\frac{f(M_w)\,M_w}{f(M_u)\,M_u}\right]^{-1}, \tag{2.2}$$

where δ is the deflection angle of detonation surface caused by a shock-shock, M_w is the Mach number of the disturbed detonation, M_u is the Mach number of the undisturbed detonation, and

$$f(M) = \exp\left\{-\int \frac{2M\,\mathrm{d}M}{[M^2-(\gamma_1/\gamma_0)]\,K(M)}\right\}, \tag{2.3}$$

where $K(M)$ is well-defined in the reactive CCW relation (Li & Ben-Dor 1998). As M_{CJ}, γ_0, γ_1 are known for a certain mixture, (2.2) can be rewritten as the following function for convenience:

$$\delta = F_{S\text{-}S}(M_u, M_w). \tag{2.4}$$

With $\delta = \varphi$, $M_u = M_i$ and $M_w = M_m$, M_m can be expressed as

$$M_m = F_{CCW}(M_i, \varphi). \tag{2.5}$$

According to geometric relations (see Appendix A), M_m can be expressed as

$$M_m = M_i \cos\chi / \cos(\chi+\varphi). \tag{2.6}$$

Thus for a certain mixture, the triple-point trajectory angle in the equilibrium limit (χ) can be obtained from

$$\chi = G_{3S}(M_i, \varphi) \tag{2.7}$$

or

$$\chi = G_{CCW}(M_i, \varphi). \tag{2.8}$$

https://doi.org/10.1017/jfm.2026.11751 Published online by Cambridge University Press

Wedge	φ_1 (deg.)	φ_2 (deg.)	S_1 (mm)	S_2 (mm)	χ_1 (deg.)	α_m
A1	15	30	56.0	150.0	7.0	1.070
A2	15	30	96.6	130.0	—	—
A3	15	30	135.2	110.0	—	—
A4	15	30	173.9	90.0	—	—
B1	20	35	43.9	130.8	5.4	1.102
B2	20	35	73.1	113.3	—	—
B3	20	35	102.3	95.9	—	—
B4	20	35	131.6	78.5	—	—
C1	25	40	106.5	70.0	3.4	1.135

Table 1. Details of nine concave wedges and parameters of Mach stem m_1 obtained from the experiment: φ_1 is the angle of the first wedge; φ_2 is the angle of the second wedge; S_1 is the length of the first surface; $S_2$is the length of the second surface; χ_1 is the triple-point trajectory angle in the equilibrium limit of MR1; $\alpha_m$is the overdrive degree of m_1.

The theoretical model used in this study is relatively simplified, as it neglects both the cellular structure and the finite detonation thickness. Li *et al.* (2015) and Li & Lee (2016) studied the MR of ZND detonations and cellular detonations, respectively. They indicated that the MR of a cellular detonation behaves essentially in the same way as a planar ZND detonation wave. The cellular instabilities, however, determine the local wave configuration, thereby inducing fluctuations in the flow field of MR. Meanwhile, near the critical angle (φ_c), an unstable cellular structure may promote the transition from RR to MR. Within a cell length, the strength of the shock front varies typically as approximately $1.3-0.8V_{CJ}$ (Li & Lee 2016), where V_{CJ} is the CJ detonation wave velocity. The curvature of the front also changes during the cell cycle. The angle of incidence of the detonation front on the wedge changes depending on the phase of the cell cycle, thus either RR or MR can occur. According to Li *et al.* (2025), the curvature of the Mach stem in the cellular structure significantly influences the type of reflection, resulting in alternating MR and RR over wedges. In general, when $\varphi < \varphi_c$, the overall characteristics of MR are unaffected by cellular instability, while cellular instability significantly affects the transition from MR to RR. Table 1 presents the wedge angles in this study. Li *et al.* (2018) indicated that the theoretical model is particularly applicable when $\varphi < 30°$, but deviations occur when $\varphi > 30°$. Thus most of the situations described in this paper, e.g. MR1 ($\varphi = \varphi_1 < 30°$) and MR2 ($\varphi = \Delta\varphi = 15°$), fall within the theory's scope of application. In this paper, we focus primarily on the MR characteristic rather than on the transition between MR and RR. Thereby, the limitation of the theoretical model in predicting φ_c does not affect the conclusion drawn in this study. Subsubsection 4.3.3 briefly discusses the possible influence of the MR-RR transition angle on MR3.

3. Experimental details

Experiments were carried out in a channel with inner cross-section dimensions 110 mm × 15 mm. An obstructed channel (2500 mm long) was used as the driver section. A 1 m long fence-like obstacle configuration was placed downstream of the igniter to accelerate the flame propagation and ensure the formation of a CJ detonation wave before the test section. The mixture used in the driver section is $2H_2 + O_2 + 2Ar$, with the same pressure as the test section. More details of the detonation channel can be found in our previous studies (Wang & Ma 2024; Zhou *et al.* 2025). A well-established detonation wave could be formed in this module. The test section was a 500 mm long channel, with

https://doi.org/10.1017/jfm.2026.11751 Published online by Cambridge University Press

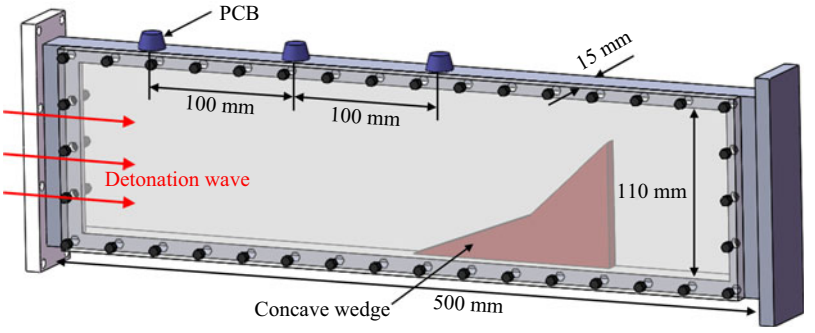


Figure 3. Test section of the experimental set-up.

one removable lateral wall (see figure 3). As mentioned by Fay (1959), detonation waves with velocity deficits could occur in a narrow channel. Considering that the velocity deficit has a significant impact on MR (Zhou *et al.* 2024), three pressure transducers (model PCB 113B24) were mounted downstream of the entrance of the test section. The distances between the entrance and transducers are 100 , 200 and 300 mm. Therefore, the velocity (or Mach number) of the incident detonation wave could be determined. A threshold value $\alpha_i = 0.95$ was found above which the MR characteristics of a detonation agree well with those of a CJ detonation (Zhou *et al.* 2024). In this study, since α_i is larger than 0.95, the influence of velocity deficits can be neglected. Nine concave wedges were employed in this study, the details of which are given in table 1.

Tests were conducted with stoichiometric hydrogen–oxygen diluted with 40 % argon, e.g. $2H_2 + O_2 + 2Ar$, at various initial pressures (p_0). The three components were injected into an individual vessel in turn to prepare the detonable mixture. For each shot, the channel was evacuated and filled with the mixture. Ignition was accomplished by a sparking plug with energy 300 mJ. The whole cellular structure over the double wedge was recorded on a 0.3 mm thickness soot foil.

4. Results and discussions

4.1. *The MR over the first wedge surface*

Figure 4 presents a series of typical soot foil records over various double wedges, in which the MR processes illustrated in figure 2 can be observed. The Mach stem is an overdriven detonation wave, which leads to finer and distorted cellular structures on the soot foils. Therefore, the incident wave region and Mach stem region are separated by an obvious boundary line, i.e. the triple-point trajectory can be recognised (see dashed lines in figure 4). More typical soot foil records and the detection of cellular characteristics are presented in Appendix B.

Over the first surface, a classical MR configuration (MR1) occurs, consisting of a CJ incident wave i, a reflection wave r, and a Mach stem m. Thus MR1 corresponds to the conventional mode over a straight wedge. The cell size of the incident wave has been identified as an appropriate length scale for characterising the MR of detonation waves (Li *et al.* 2018; Zhou *et al.* 2024). Figure 5(a) shows the measured cell size under the CJ condition (λ_{CJ}). Figure 6(a) presents the trajectory of T_1 normalised by λ_{CJ} (where h_1 is the height of m_1, and L_1 is the travel of m_1). The normalised triple-point trajectories at different initial pressures nearly collapse into a single curve, exhibiting the localised self-similarity. As reported by Li *et al.* (2018), the frozen limit exists within approximately $L_1 = (3{-}5)\lambda_{CJ}$, and the equilibrium limit occurs at $L_1 = (6{-}10)\lambda_{CJ}$. In this study, the

https://doi.org/10.1017/jfm.2026.11751 Published online by Cambridge University Press

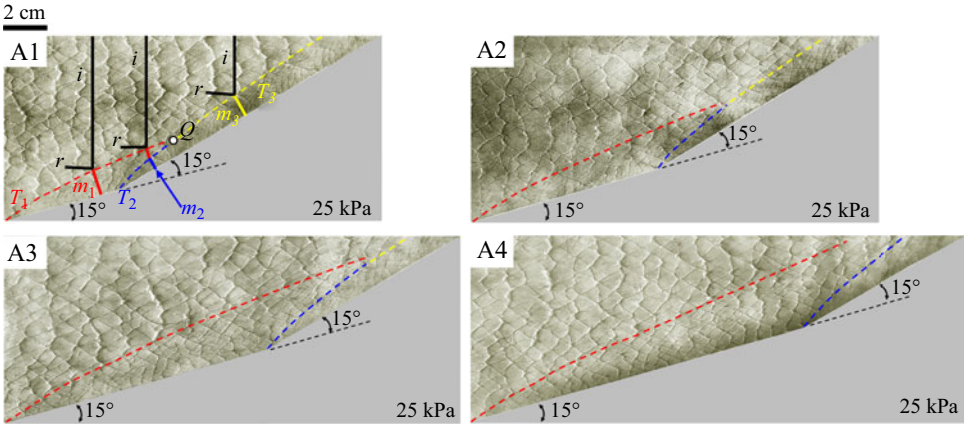


Figure 4. Typical soot foil records of wedges A1–A4.

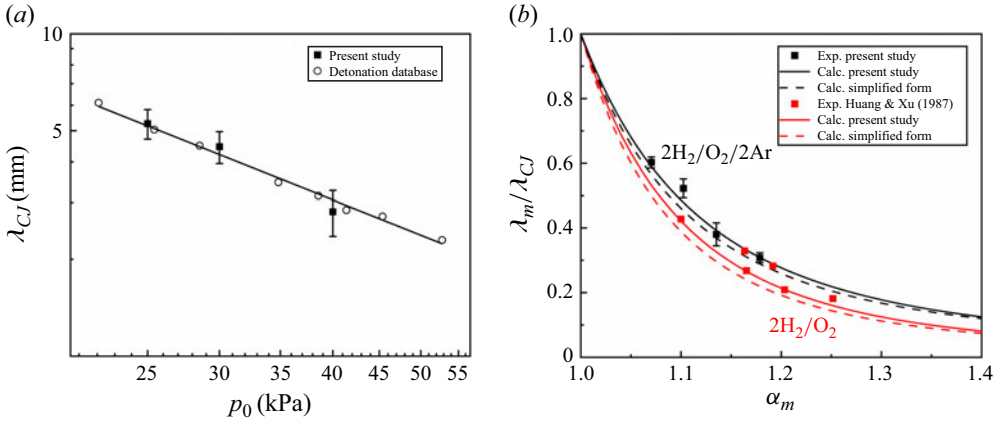


Figure 5. Measured cell size behind (*a*) incident detonation wave i, (*b*) Mach stem m_1. In (*b*), the theoretical results are calculated using (4.3) and (4.5), where black represents $2H_2 + O_2 + 2Ar$, and red represents $2H_2 + O_2$.

frozen limit is found to exist within approximately $L_1 = 5\lambda_{CJ}$, and the equilibrium limit is found to occur at $L_1 = 10\lambda_{CJ}$. The triple-point trajectory angle in the frozen limit (θ_1) is 16.5° for the case $\varphi_1 = 15°$, which is consistent with the prediction of the non-reactive theories (Whitham 1957; Ben-Dor 2007). As shown in figure 6(*b*), when the wedge angle is less than 30°, the asymptotic triple-point trajectory angle in the equilibrium limit (χ_1) is in agreement with the predictions of (2.7) and (2.8). However, χ_1 deviates from the theoretical results when the wedge is larger than 30°, indicating the limitations of these theories based on the simplified model in § 2.

As reported by Li *et al.* (2018) and Zhou *et al.* (2024), the overdrive degree of m_1 ($\alpha_m = M_{m1}/M_{CJ}$, where M_{m1} is the Mach number of a straight Mach stem perpendicular to the wedge surface) remains approximately constant in the far field. According to (2.6), α_m can be expressed as

$$\alpha_m = \alpha_i \cos\chi_1 / \cos(\chi_1 + \varphi_1), \tag{4.1}$$

where α_i is the overdrive degree of the incident detonation wave (for MR1, $\alpha_i = 1$). Table 1 presents α_m with different φ_1. Desbordes (1988) indicated that the cell size drastically

https://doi.org/10.1017/jfm.2026.11751 Published online by Cambridge University Press

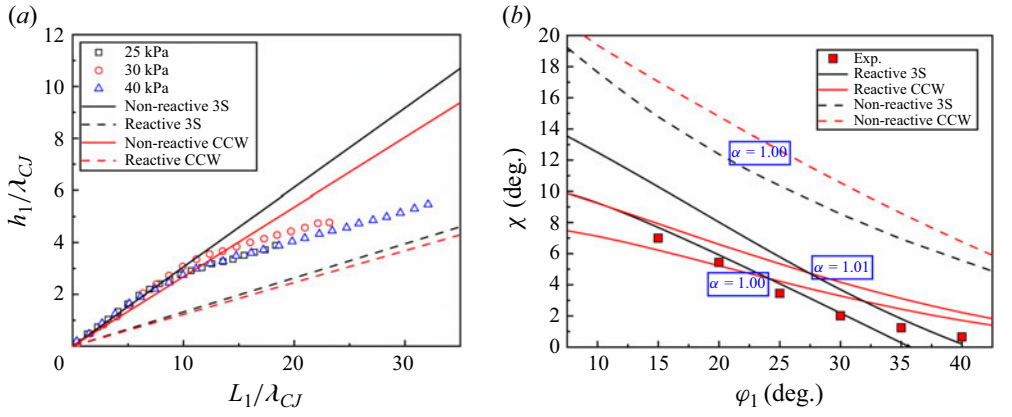


Figure 6. (*a*) Trajectory of T_1 for the case $\varphi_1 = 15°$. (*b*) Asymptotic triple-point trajectory angle in the equilibrium limit of MR1.

decreases as the overdrive degree increases. Since the ratio of the cell size to the chemical induction zone length remains constant when the overdrive degree changes (Huang & Xu 1987), the cell size λ_m behind m_1 in the far field can be expressed as

$$\frac{\lambda_m}{\lambda_{CJ}} \approx \frac{L_{i,m}}{L_{i,CJ}} = \frac{u_m}{u_{CJ}} \frac{t_{ig,m}}{t_{ig,CJ}}, \tag{4.2}$$

where L_i is the induction zone length, u is the flow velocity behind the leading shock in the shock-attached frame of reference, t_{ig} is the chemical induction time, and the subscripts m and CJ represent m_1 and the CJ detonation wave, respectively. Using the normal shock wave relations, the ratio u_m/u_{CJ} can be expressed by α_m and M_{CJ}. Considering $t_{ig} \sim \rho_s^{-1} \exp(E_a/RT_s)$ (Soloukhin & Ragland 1969; Desbordes 1988) and $M_{CJ}^2 \gg (\gamma_0 - 1)/2\gamma_0$, we can get

$$\frac{\lambda_m}{\lambda_{CJ}} \approx \frac{\beta^2}{\alpha_m^3} \exp\left[\frac{E_a}{RT_{s,CJ}}(\beta^{-1} - 1)\right], \tag{4.3}$$

$$\beta = \frac{2M_{CJ}^{-2} + (\gamma_0 - 1)\alpha_m^2}{2M_{CJ}^{-2} + (\gamma_0 - 1)}, \tag{4.4}$$

where ρ_s and T_s are the flow density and temperature behind the leading shock, respectively, and $E_a/RT_{s,CJ}$ is the normalised activation energy of a CJ detonation wave. With a large M_{CJ} ($2M_{CJ}^{-2} \ll \gamma_0 - 1$ and $2M_{CJ}^{-2} \ll (\gamma_0 - 1)\alpha_m^2$), (4.3) can be further simplified to

$$\frac{\lambda_m}{\lambda_{CJ}} \approx \alpha_m \exp\left[\frac{E_a}{RT_{s,CJ}}(\alpha_m^{-2} - 1)\right]. \tag{4.5}$$

The details of (4.2)–(4.5) are presented in Appendix C; $E_a/RT_{s,CJ}$ can be calculated based on a procedure proposed by Ng (2005), and M_{CJ} and γ_0 can be obtained via the Shock and Detonation Toolbox in Cantera with the GRI30 detailed chemical mechanism. The mixture parameters are listed in table 2. In this study, the data for λ_m were obtained from cells located near the wedge surface, where the Mach stem is basically perpendicular to the wedge surface. The results in figure 5(*b*) indicate that the relation between λ_m/λ_{CJ} and α_m can be well predicted by (4.3). Obviously, M_{CJ} is not large enough, thereby causing (4.5) to underestimate λ_m/λ_{CJ}.

https://doi.org/10.1017/jfm.2026.11751 Published online by Cambridge University Press

p_0 (kPa)	V_{CJ} (m s^{-1})	M_{CJ}	γ_0	γ_1	$E_a/RT_{s,CJ}$
20	1981.4	4.986	1.478	1.311	5.040
25	1990.3	5.009	1.478	1.310	5.025
30	1997.6	5.027	1.478	1.309	5.019
40	2009.3	5.056	1.478	1.307	5.012

Table 2. Properties of $2H_2 + O_2 + 2Ar$ mixture at 298 K, where V_{CJ} is the CJ detonation wave velocity.

4.2. *The MR of an overdriven detonation wave*

As the Mach stem m_1 encounters the second wedge, a new MR configuration (MR2) can be observed. In this study, the first wedge is sufficiently long to ensure that MR1 approaches the equilibrium limit before encountering the second wedge. In the equilibrium limit, m_1 can be regarded as a relatively stable overdriven detonation wave (Li *et al.* 2018; Zhou *et al.* 2024). The overdrive degree of m_1(α_m) is presented in table 1. Since m_1 acts as the incident wave, MR2 corresponds to the MR of an overdriven detonation wave. A newly formed Mach stem m_2, exhibiting a finer cellular structure, appears near the second wedge surface (see figure 4).

4.2.1. *Fine structure of the curved Mach stem*

For MR1, the fine structure of m_1 was neglected, since the availability of the straight Mach stem assumption in predicting χ_1 and M_{m1} is widely proved over a single wedge (Li *et al.* 1997, 2018; Li & Ben-Dor 1998; Zhou *et al.* 2024). However, as reported by Fortin *et al.* (2015), the Mach stem is curved, and instead of a single reflected shock, a series of reflected compression waves could be observed. They also indicated that the triple point is a diffused region rather than a sharp point. Thus the compression waves coalesce incompletely, and instead of forming a discontinuous shock wave, a band of compression waves near the triple point appears. Up to now, there are no appropriate explanations for the curved Mach stem in MR of gaseous detonations. Bdzil & Short (2017) indicated that for MR in condensed-phase detonations, the reaction-zone heat-release flow dynamics can itself turn the flow without a reflected shock being required for that purpose. They found that for smaller wedge angles, the reflected waves are compressions and not shocks in the reaction zone. For gaseous detonations, the curved Mach stem can also be ascribed to the reaction zone behind the leading shock. Generally, it is inappropriate to regard m_1 as a straight line for MR2.

Figure 7 shows the model of a curved Mach stem while the reflected shock wave is replaced by a series of compression waves. In this model, the point T_1 is defined as the intersection of the first reflected compression wave and i. The separated compression waves in the vicinity of T_1 lead to the formation of a concave curved Mach stem. Two parts of the Mach stem are introduced, i.e. a straight Mach stem (MS_s) perpendicular to the wedge surface, and a concave curved Mach stem (MS_c) near T_1. The point P is defined as the boundary between MS_s and MS_c. There is no discontinuity along the detonation front at T_1, and the disturbances that exist on the Mach stem can be regarded as simple waves. Therefore, according to the CCW theory (Whitham 1957), the variations of the Mach number (M) and the deflection angle of detonation surface (δ) along the Mach stem can be expressed as

$$\delta = \int_{M_i}^{M} \frac{1}{A(M)\, c(M)}\, \mathrm{d}M, \tag{4.6}$$

https://doi.org/10.1017/jfm.2026.11751 Published online by Cambridge University Press

φ_1 (deg.)	Exp.	Calc. by (4.6)	Relative error (%)	Calc. by 3S	Relative error (%)	Calc. by CCW	Relative error (%)
15	1.070	1.064	−0.56	1.075	0.47	1.066	−0.37
20	1.102	1.092	−0.91	1.105	0.27	1.101	−0.09
25	1.135	1.124	−0.97	1.140	0.44	1.143	0.68

Table 3. Experimental and theoretical results for α_m.

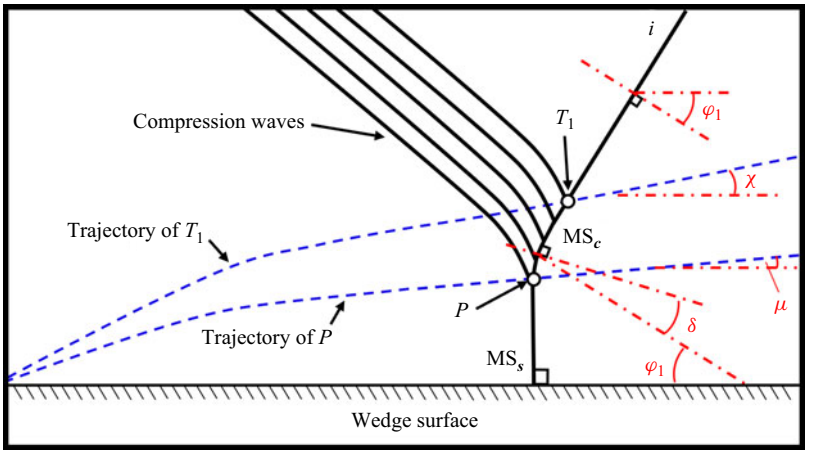


Figure 7. The model of a curved Mach stem. φ_1: wedge angle; χ: trajectory angle of T_1; μ: trajectory angle of P; δ: deflection angle of detonation surface.

where $A(M)$ and $c(M)$ can be obtained from

$$\frac{2M\,\mathrm{d}M}{[M^2-(\gamma_1/\gamma_0)]\,K(M)}+\frac{\mathrm{d}A}{A}=0, \tag{4.7}$$

$$c=\sqrt{-\frac{M}{A'(M)\,A}}, \tag{4.8}$$

where A is a quantity that represents area, and A' is the derivative of A with respect to M (see details in Whitham 1957).The expression for $K(M)$ can be found in Li & Ben-Dor (1998). For MS_s, M_{m1} can be calculated with $\delta=\varphi_1$. The relative error between the experimental result and the prediction of (4.6) is less than 1 % (see table 3).

The soot foil records also indicate the occurrence of a curved Mach stem. According to (4.3), the cell size behind the detonation wave decreases rapidly with the increase of the overdrive degree. The Mach stem curvature influences the overdrive degree and the incident angle $(\pi/2-(\varphi_1-\delta))$ of different segments of the Mach stem, thereby influencing the cellular structures in corresponding regions. Figure 8 illustrates the cellular structures observed in three distinct detonation regions of MR1. It should be noted that the detonation cells are selected in the far field (equilibrium limit) due to the partial absence of cellular structure in the frozen limit. The absence of cells can be ascribed to the high overdrive degree of the Mach stem in the frozen limit (Li *et al.* 2018; Zhou *et al.* 2024). The incident wave i can be approximated as a plane wave front with a regular quadrilateral cellular structure (see figure 8*a*). The cellular structure of MS_s is similar to that of i, but exhibits a smaller cell size due to a higher overdrive degree (see figure 8*a*). In the case of

https://doi.org/10.1017/jfm.2026.11751 Published online by Cambridge University Press

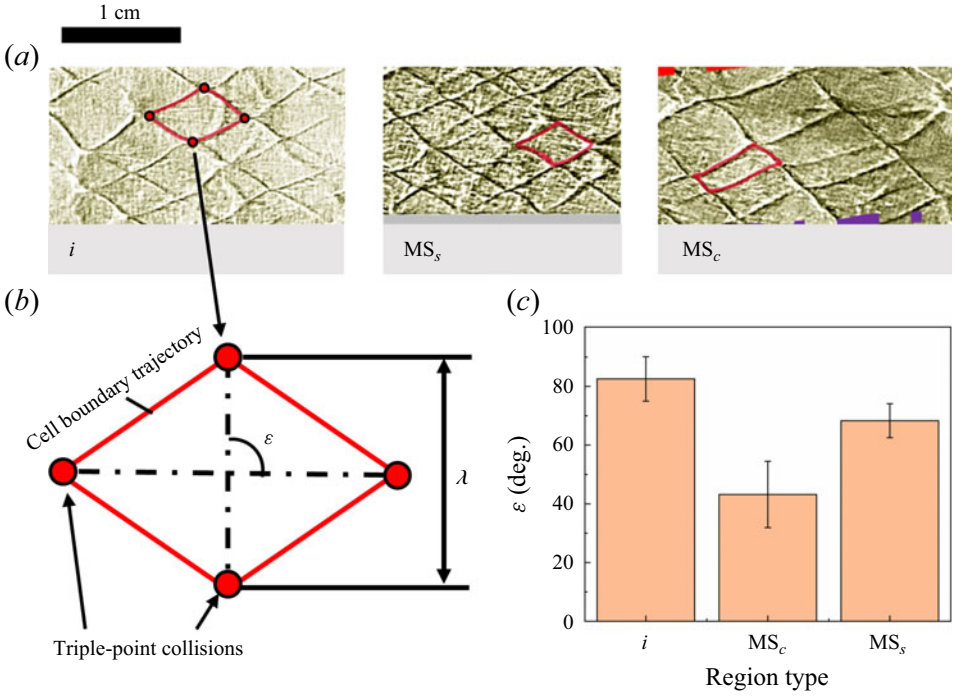


Figure 8. (*a*) Typical cellular structures in three regions. (*b*) Sketch of cellular structure. (*c*) Characteristic angle ε in three regions.

MS$_c$, a distorted cellular structure can be observed (see figure 8*a*). Meagher *et al.* (2023) indicated that the deflecting direction of the cell is related to the direction of propagation of the Mach stem over the cell life. Thus the distortion can be attributed to the curvature of MS$_c$. Meanwhile, the cell size of MS$_c$ is larger than that of MS$_s$ due to the lower overdrive degree. A characteristic angle ε is introduced to quantitatively describe the deformation (see figure 8*b*). Triple-point collision locations, which correspond to the intersections of cell boundary trajectories, are identified to obtain ε. As shown in figure 8(*c*), ε of *i* and MS$_s$ are generally larger than 60°, while ε of MS$_c$ is close to 40° due to the deformation of cells.

The above discussions are primarily based on the two-dimensional cell pattern of the cellular detonation. Essentially, the cellular detonation wave is three-dimensional. In a rectangular channel, two propagation modes of cellular detonation waves can be identified, i.e. rectangular mode and diagonal mode (Hanana & Lefebvre 2001). According to Strehlow (1969), the rectangular mode is the most common structure of cellular detonation waves, especially in a rectangular channel with large aspect ratio such as the one utilised in this study. The rectangular structure consists of orthogonal waves travelling independently from each another. The soot record in this case shows the classical diamond detonation cell exhibiting 'slapping waves'. The slapping waves appear as light stripes perpendicular to the propagation direction of the detonation wave in smoke foils. According to Hanana & Lefebvre (2001), the lines of triple points develop two pairs of rectangular surfaces orthogonal to one another. Those surfaces reflect against the tube wall and are responsible for the slapping waves. Figure 9 shows the slapping wave (see the cyan line) recorded by soot foils. For MS$_c$, the slapping waves bend anticlockwise, corresponding to the concave Mach stem. For MS$_s$, new slapping wave stripes can be observed between the

https://doi.org/10.1017/jfm.2026.11751 Published online by Cambridge University Press

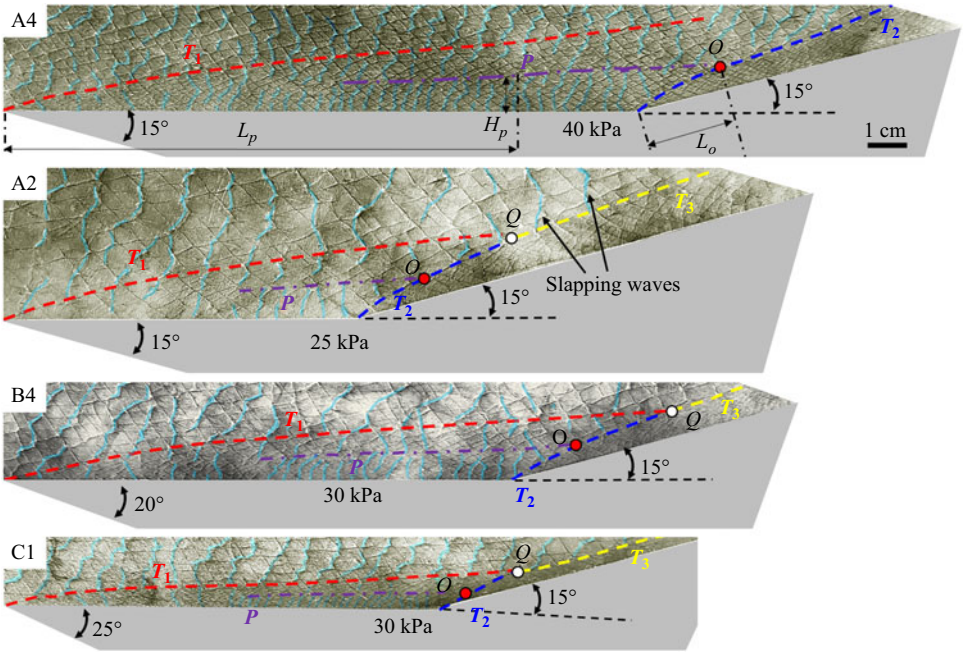


Figure 9. Typical soot foil records of the curved Mach stem structure and the slapping wave. The slapping wave is marked by the cyan line; $L_P$is travel of P, H_P is height of P, and L_O is the distance of O along the second wedge surface.

original stripes, indicating the generation of new cells (or transverse waves). This newly formed slapping wave is basically perpendicular to the wedge surface, corresponding to the straight Mach stem perpendicular to the wedge surface. Lin *et al.* (2018) indicated that the new slapping waves will only appear when α_m is relatively large. Thus MS_s is stronger than MS_c, which is consistent with the conclusion derived from the two-dimensional analysis. It should be noted that the determination of T_1 via soot foil records in § 4.1 is not in conflict with the new model, given the clear differences of the cellular structure among three regions. For the curved Mach stem model, the trajectory of T_1 can still be obtained by comparing the cell size and shape. More soot foil records are presented in Appendix B.

To investigate the influence of curved m_1 on MR2, the characterisations of the boundary point P and the intersection O are essential. According to the soot foil records, P can be determined via the cellular structure and the newly formed slapping wave. Figure 9 shows the trajectory of P on the soot foil. In the frozen limit of MR1, the trajectory of P is difficult to determine from the soot foil records due to the partial absence of cellular structure. Thus the trajectory of P is discernible only in the far field. Figure 10 shows the normalised trajectory of P (where H_P is the height, and L_P is the travel). For a certain φ_1, the normalised trajectories of P with different p_0 seem to collapse into a single line. Thereby, the angle μ between the trajectory of P and the first surface, which is solely related to φ_1, can be measured, i.e. $\varphi = 15°$, $\mu = 3.2°$; $\varphi = 20°$, $\mu = 2.4°$; $\varphi = 25°$, $\mu = 1.3°$. Meanwhile, the intercept of the normalised trajectory remains approximately unity with different φ_1 and p_0 (see figure 10). Since P should originate at the apex of the wedge, the intercept represents an experimental value without physical meaning. The normalised trajectory of P can be expressed as

$$H_P/\lambda_m = \tan(\mu)\,(L_P/\lambda_m) + 1. \tag{4.9}$$

https://doi.org/10.1017/jfm.2026.11751 Published online by Cambridge University Press

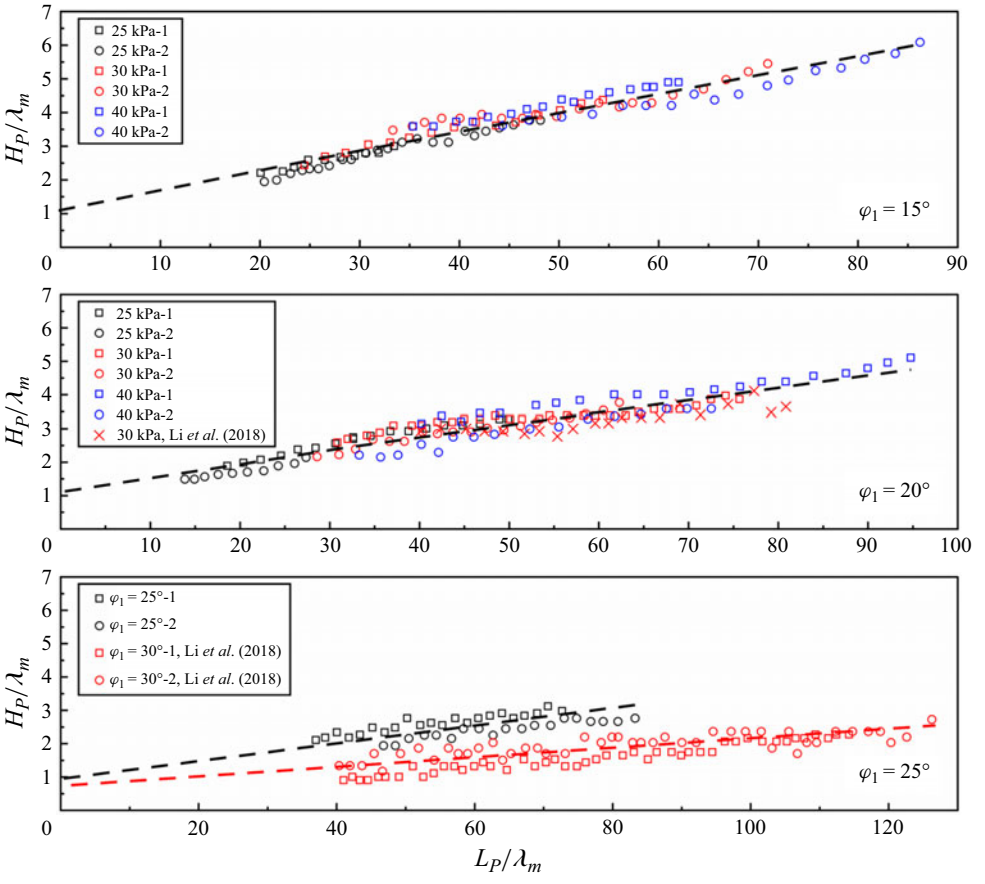


Figure 10. Normalised trajectory of P.

Notably, the intercept obtained in the present study is limited to the mixture $2H_2 + O_2 + 2Ar$. The intercept may vary for different mixtures.

Before the intersection of P and T_2 (O), MS_s serves as the incident wave in MR2. Thereafter, MS_c serves as the incident wave in MR2. Figure 11 presents the interaction process between T_1, T_2 and P, which indicates that the trajectory of T_2 before O can be approximated to a straight line. Thus before O, the angle between the trajectory of T_2 and the second surface can be regard as θ_2. Combining with (4.9), the location of point O can be calculated by the geometrical expression

$$\frac{L_O}{\lambda_m} = B\frac{\lambda_{CJ}}{\lambda_m}\frac{S_1}{\lambda_{CJ}} + \frac{B}{\tan\mu}, \tag{4.10}$$

$$B = \frac{\sin(\Delta\varphi + \theta_2) - \sin(\Delta\varphi + \theta_2 - \mu)}{\sin(\Delta\varphi + \theta_2 - \mu)\cos(\Delta\varphi + \theta_2 - \mu)}\cos\theta_2, \tag{4.11}$$

where L_O is the distance of O along the second wedge surface, and $\Delta\varphi = \varphi_2 - \varphi_1$. The cell size ratio λ_{CJ}/λ_m can be calculated by (4.3). For a certain mixture, λ_{CJ}/λ_m and μ are functions of φ_1. Here, θ_2 is a function of φ_1 and φ_2. Thus L_O/λ_m can be expressed as $L_O/\lambda_m = f_O(\varphi_1, \varphi_2, S_1/\lambda_{CJ})$. By eliminating the influence of p_0, the normalised wedge length S_1/λ_{CJ} serves as a more appropriate parameter for characterising the scale of the first wedge compared to the wedge length S_1. Also, L_O/λ_m is determined by the geometric

https://doi.org/10.1017/jfm.2026.11751 Published online by Cambridge University Press

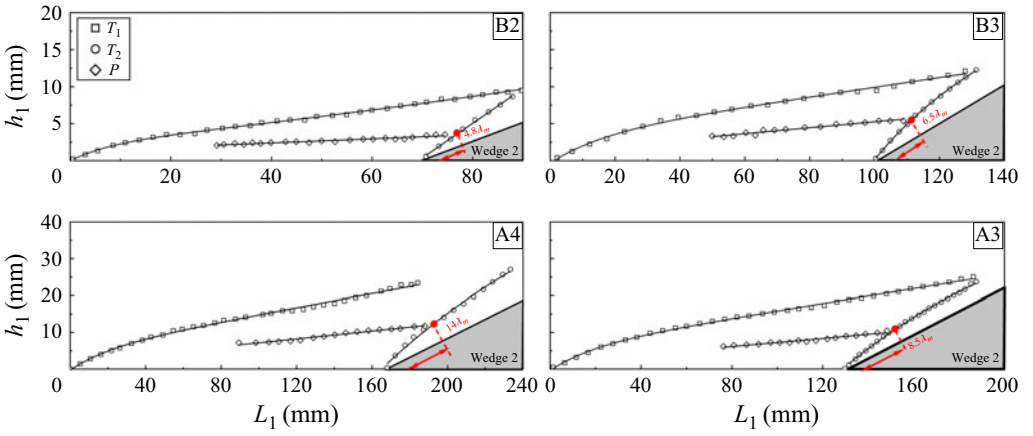


Figure 11. Typical trajectories of T_1, T_2 and P for $p_0 = 40$ kPa.

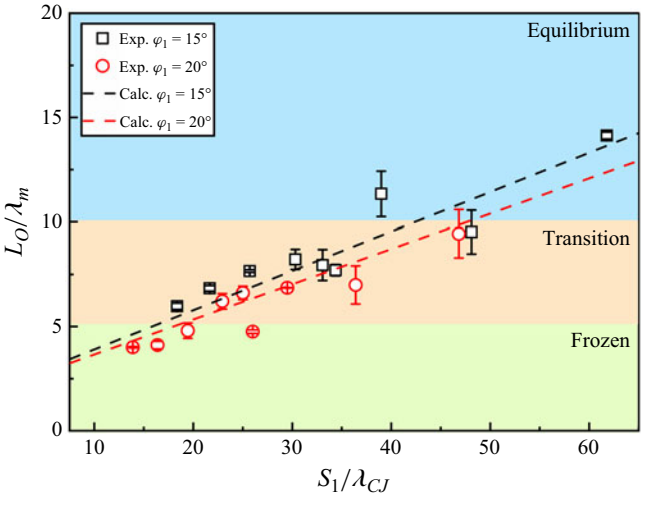


Figure 12. Normalised distance of O as a function of S_1/λ_{CJ}. The theoretical results are calculated using (4.10). Here, $\Delta\varphi = 15°$ and $\theta_2 = 16.5°$.

construction of the double wedge. Figure 12 illustrates the experimental and theoretical results of L_O/λ_m against S_1/λ_{CJ} over different double wedges. The experimental result is well consistent with the prediction of (4.10). Since the trajectory of P is discernible only in the equilibrium limit, (4.10) is only appropriate for the cases $S_1/\lambda_{CJ} > 10$.

4.2.2. *Triple-point trajectory and triple-point trajectory angle of MR2*

Figure 13 presents the theoretical prediction of the triple-point trajectory angle base on the straight Mach stem assumption. The results obtained using the non-reactive theories (Whitham 1957; von Neumann 1963) and the reactive theories correspond to θ and χ, respectively. The theoretical results indicate that the initial pressure p_0 has a negligible impact on the triple-point trajectory angle. For the non-reactive cases, the triple-point trajectory angle is insensitive to α. However, for the reactive cases, the triple-point trajectory angle increases rapidly with α. Since the curved Mach stem model is introduced

https://doi.org/10.1017/jfm.2026.11751 Published online by Cambridge University Press

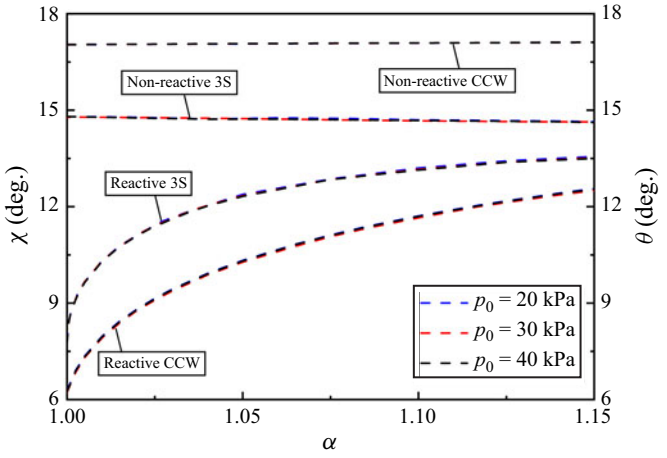


Figure 13. Theoretical prediction of the relationship between the triple-point trajectory angle and the overdrive degree of the incident wave. The non-reactive theories and the reactive theories correspond to θ and χ, respectively.

in § 4.2.1, the experimental results can be inconsistent with the theoretical results presented in figure 13, especially for the triple-point trajectory after O.

According to the curved Mach stem model, MS_s serves as the incident wave near the apex of the second wedge (before O). Thus the classical reactive theories based on the straight Mach stem assumption (see § 2) are still available for MR2 in the near field (before O). Figure 14 shows the trajectory of T_2 normalised by λ_m (where h_2 is the height of m_2, and L_2 is the travel of m_2). The triple-point trajectory remains straight near the apex of the second wedge, demonstrating behaviour consistent with the 'frozen limit'. The cell size of the incident wave (λ_m) continues to serve as a characteristic length scale for the MR of an overdriven detonation wave. The normalised trajectory of T_2 in the frozen limit is nearly identical to that of T_1. Figure 15(a) illustrates the triple-point trajectory angle in the frozen limit (θ_2) against the normalised length of the first wedge S_1/λ_{CJ}. The experimental results indicate that θ_2 approaches θ_1 obtained from a single wedge with $\varphi_1 = 15°$, which is in good agreement with the prediction in figure 13.

The experimental results indicate that unlike T_1, the trajectory of T_2 in the far field (after O) is slightly curved, and they deviate from each other under different conditions (see figure 14). Meanwhile, the trajectory of T_2 in the far field is significantly inconsistent with the prediction based on the straight Mach stem assumption. In the far field (after O), if the trajectory of T_2 is approximated by a straight line, then it forms an angle χ_2 with the second wedge surface; χ_2 can be used to characterise the behaviour of MR2 influenced by MS_c. For MR1, the equilibrium limit is found to occur at $L_1 = 10\lambda_{CJ}$ (see figure 6a). Thus in this study, χ_2 was obtained from the triple-point trajectory between $L_2 = 10\lambda_m$ (or $L_2 = L_O$, if $L_O/\lambda_m > 10$) and the point Q. Figure 15(b) illustrates χ_2 against S_1/λ_{CJ}. According to the reactive theories, χ_2, as the asymptotic triple-point trajectory angle of an overdriven detonation wave, is expected to be significantly larger than that of a CJ detonation (see figure 13). However, the experimental results indicate that χ_2 is generally smaller than χ obtained from a single wedge with $\varphi = 15°$, and larger than χ obtained from a single wedge with $\varphi = \varphi_2$. After O, MS_c serves as the incident wave. According to (4.6), the Mach stem curvature influences the overdrive degree and the incident angle of different segments of the Mach stem. The incident angle is the angle between the detonation front and the wedge surface. Here, MS_c has a concave curvature towards the

https://doi.org/10.1017/jfm.2026.11751 Published online by Cambridge University Press

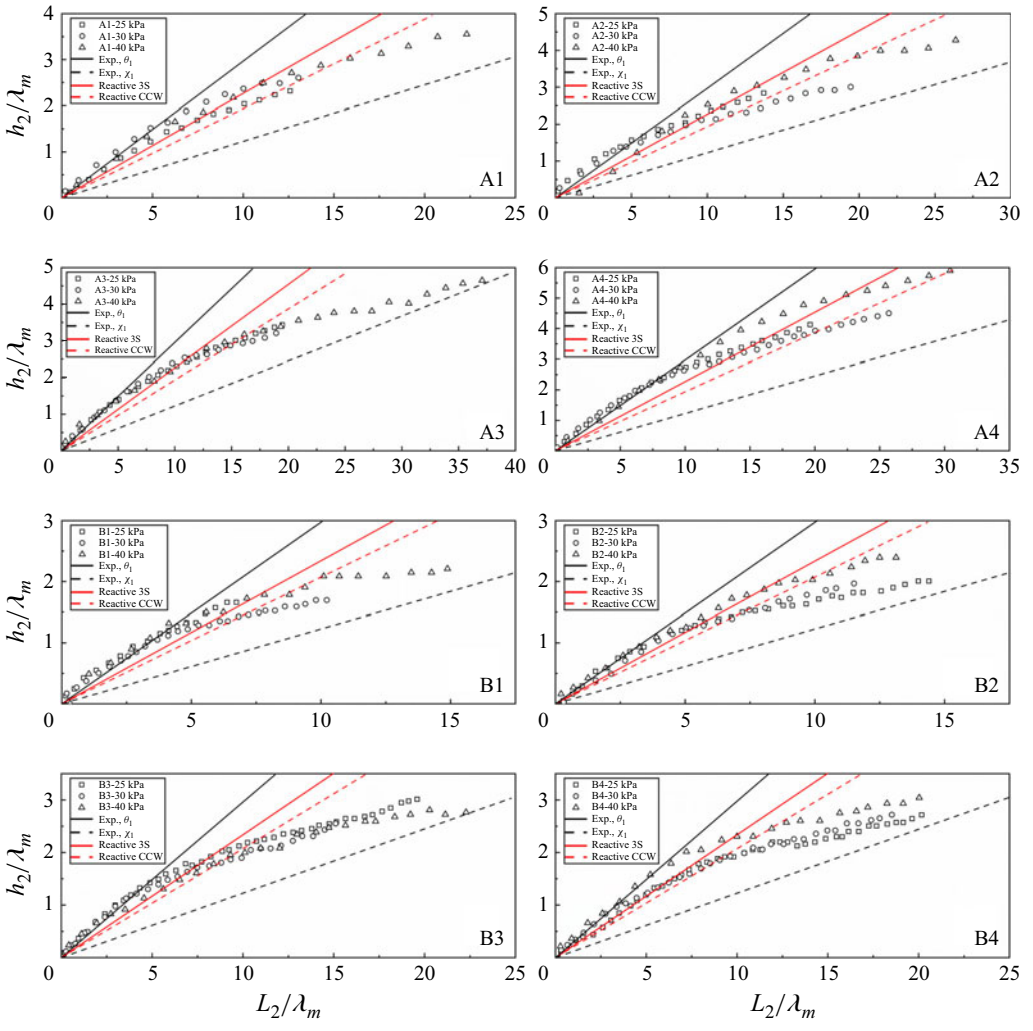


Figure 14. Normalised triple-point trajectory of MR2.

direction of propagation. The concave curvature implies a lower overdrive degree and a smaller incident angle, which consequently leads to a reduction in χ_2 (see figures 6(b) and 13). In particular, the trajectory of T_2 for wedge A4 is incomplete in the vicinity of T_1 (see figure 4), due to the limitations of the experimental set-up. The closer the location is to T_1, the more m_1 resembles i. This contributes to a larger measured χ_2 of wedge A4 compared to those of wedges A1–A3.

It is complicated to mathematically describe the curvature of MS_c accurately along the normalised distance S_1/λ_{CJ}. Meanwhile, the incident angle of MS_c varies along the second wedge surface, due to the curvature of MS_c. Thus it is difficult to directly predict χ_2 based on MS_c. Alternatively, an equivalent incident angle $\pi/2 - \Phi$ is applicable to predict χ_2, where Φ is the equivalent wedge angle. The experimental results in figure 15(b) indicate that χ_2 is influenced by the parameter of the first wedge. According to (2.6), α_m is positively correlated with φ_1. Theoretically, a larger χ_2 is expected for a higher α_m or φ_1 (see figure 13). However, the experimental results indicate that χ_2 decreases with φ_1 and S_1/λ_{CJ}. This suggests that φ_1 and S_1/λ_{CJ} can be two key factors in determining the

https://doi.org/10.1017/jfm.2026.11751 Published online by Cambridge University Press

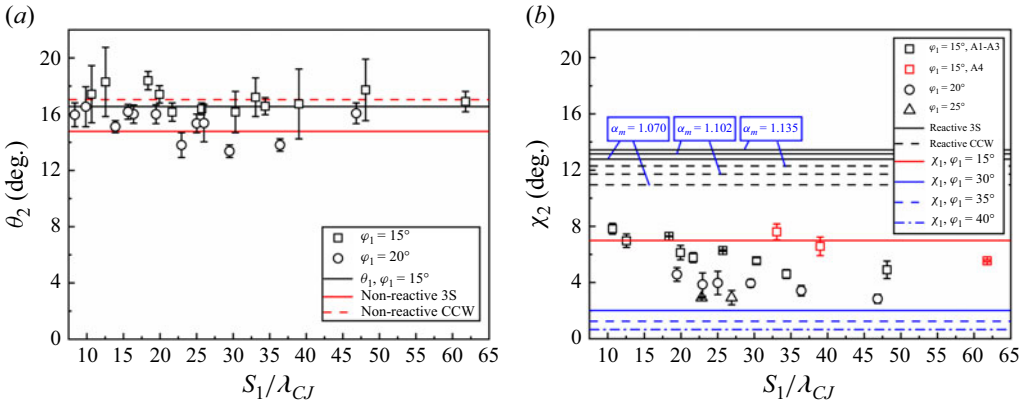


Figure 15. (*a*) Triple-point trajectory angle in the frozen limit of MR2. (*b*) Asymptotic triple-point trajectory angle in the far field of MR2.

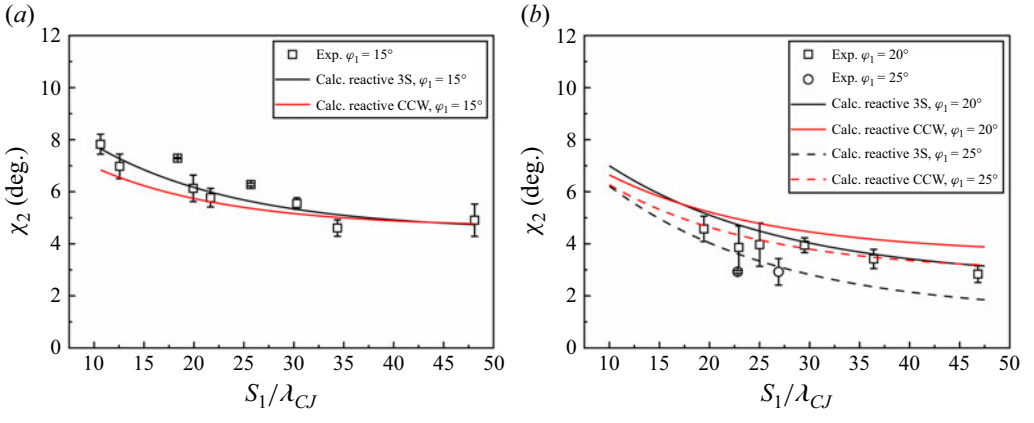


Figure 16. Asymptotic triple-point trajectory angle of MR2 predicted by the curved Mach stem model.

curvature of the Mach stem m_1. Meanwhile, the concave curvature of MS_c implies that Φ lies strictly between $\Delta\varphi$ and φ_2, i.e. $\Delta\varphi < \Phi < \varphi_2$. Therefore, Φ can be expressed by the empirical equation

$$\Phi = \frac{10\,\Delta\varphi + (S_1/\lambda_{CJ})\varphi_2}{10 + S_1/\lambda_{CJ}} = \Delta\varphi + \frac{S_1/\lambda_{CJ}}{10 + S_1/\lambda_{CJ}}\varphi_1. \tag{4.12}$$

We here clarify that (4.12) is an engineering estimate and has limitations in the applicability. The scale '10' in (4.12) corresponds to the equilibrium limit scale of $10\lambda_{CJ}$ mentioned in § 4.1. According to (4.6), the equivalent overdrive degree $\overline{\alpha}$ corresponding to Φ can be obtained from

$$\varphi_2 - \Phi = \int_{M_i}^{\overline{\alpha}M_i} \frac{1}{A(M)\,c(M)}\,\mathrm{d}M. \tag{4.13}$$

According to (2.7) and (2.8), χ_2 can be calculated by $\chi_2 = G_{3S}(\overline{\alpha}M_i, \Phi)$ or $\chi_2 = G_{CCW}(\overline{\alpha}M_i, \Phi)$. As shown in figure 16, the theoretical results using $\overline{\alpha}M_i$ and Φ are consistent with the experimental results. The reactive 3S theory is more accurate compared to the reactive CCW theory when φ_1 is large. This is coincident with the fact that the CCW

https://doi.org/10.1017/jfm.2026.11751 Published online by Cambridge University Press

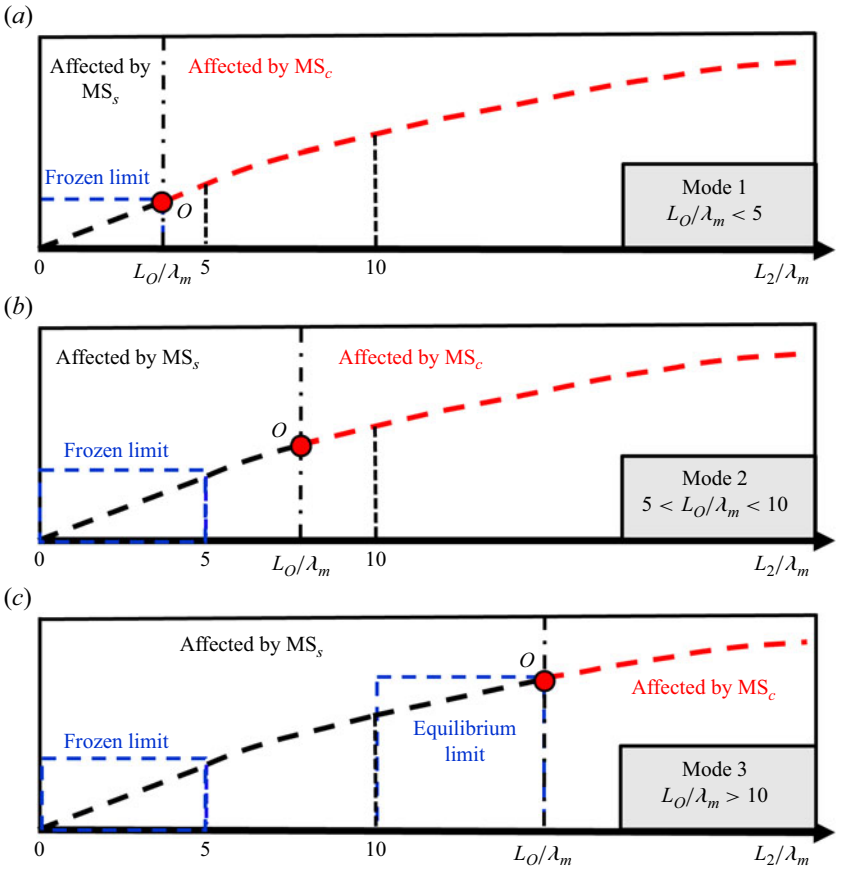


Figure 17. Three localised self-similarity modes based on the curved Mach stem model.

theory should be more accurate for weaker detonation waves since the change of weaker detonation waves is smoother (the Mach stem m_1 is stronger with a larger φ_1). When $S_1/\lambda_{CJ} < 10$, the Mach stem m_1 has not yet reached the equilibrium limit and remains unstable. Thereby, both (4.12) and (4.13) are only appropriate for the cases $S_1/\lambda_{CJ} > 10$.

4.2.3. *Localised self-similarity of MR2*

The point O, i.e. the interaction of T_2 and P, indicates the boundary between MS$_s$ and MS$_c$. When $L_2/\lambda_m < L_O/\lambda_m$, the localised self-similarity is expected, since MS$_s$ serves as the incident wave in MR2. When $L_2/\lambda_m > L_O/\lambda_m$, MS$_c$ takes over, resulting in the absence of the self-similarity. According to the experimental results of MR1 (see § 4.1), the scales of the local self-similarity are supposed to be $5\lambda_m$ (frozen limit) and $10\lambda_m$ (equilibrium limit). Therefore, different localised self-similarity modes of MR2 should occur at the distinguishing criteria of $L_O/\lambda_m = 5$ and 10 (see figure 12).

Based on the curved Mach stem model, three localised self-similarity modes can be determined theoretically. Figure 17 shows the localised self-similarity modes depending on L_O/λ_m, which can be obtained from (4.10). When $L_O/\lambda_m < 5$, the point O falls within the frozen limit (mode 1, see figure 17*a*). Serving as the incident wave in MR2, MS$_s$ only exhibits the frozen character, i.e. a straight trajectory of T_2 within $L_2/\lambda_m < L_O/\lambda_m$. Within $L_2/\lambda_m > L_O/\lambda_m$, the triple-point trajectory affected by MS$_c$ is curved. Therefore,

https://doi.org/10.1017/jfm.2026.11751 Published online by Cambridge University Press

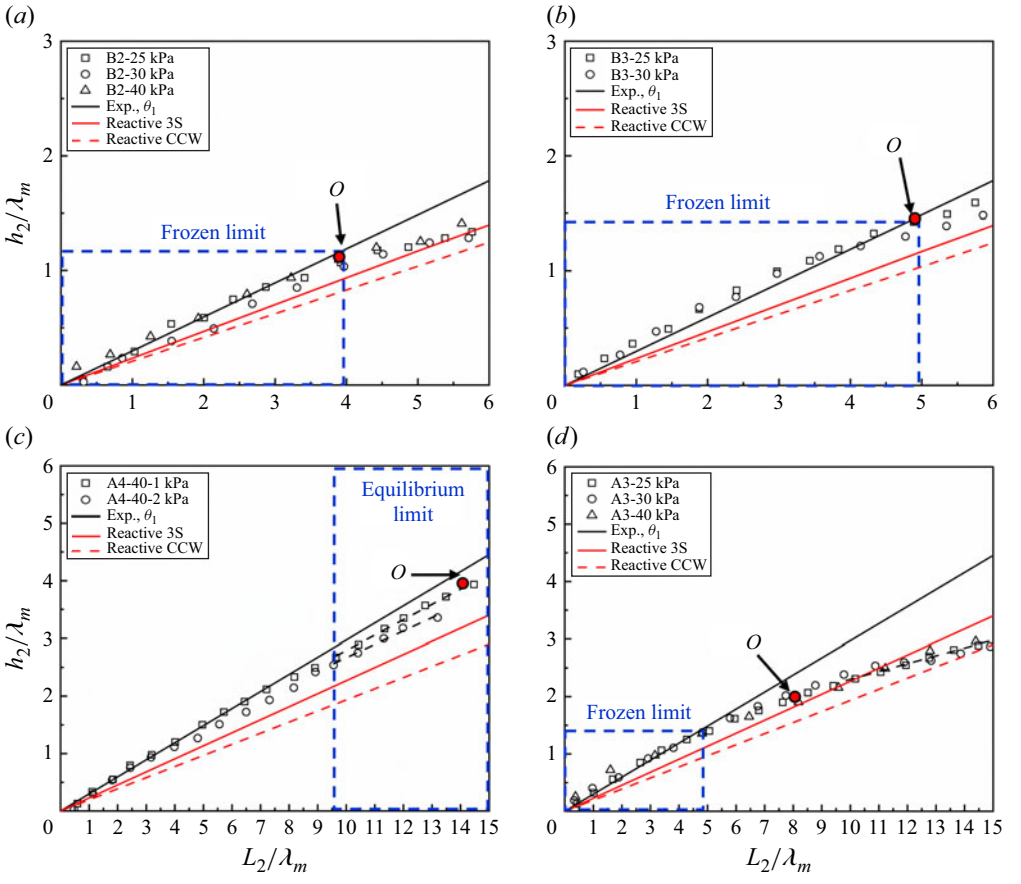


Figure 18. Typical experimental records of the three modes: (*a*) B2, mode 1, (*b*) B3, mode 2, (*c*) A4, mode 3, (*d*) A3, mode 2.

the frozen limit ends at L_O/λ_m rather than $5\lambda_m$. It is essential to clarify that the end of the frozen limit in this case is due to the emergence of MS_c instead of the classical development of MR (i.e. the local self-similarity). Thus the frozen limit of mode 1 is incomplete. When $5 < L_O/\lambda_m < 10$, the point O is located in the transition stage between two limits (mode 2, see figure 17*b*). Since MS_s serves as the incident wave until the transition stage, the frozen limit of mode 2, which exists within $L_2/\lambda_m < 5$, is complete compared to that of mode 1. Throughout the entire far field, MS_c serves as the incident wave. Therefore, the equilibrium limit caused by MS_s is absent. The asymptotic triple-point trajectory angle in the far field is solely influenced by MS_c. When $L_O/\lambda_m > 10$, the point O is located in the far field (mode 3, see figure 17*c*). In this case, MS_s, serving as the incident wave, exhibits both the frozen and equilibrium characters, i.e. the local self-similar triple-point trajectory within $L_2/\lambda_m < L_O/\lambda_m$. The trajectory of T_2 within $10 < L_2/\lambda_m < L_O/\lambda_m$ is straight, which means that the equilibrium limit caused by MS_s occurs. Since MS_s is straight, the triple-point trajectory angle within $10 < L_2/\lambda_m < L_O/\lambda_m$ can be calculated by the reactive theories. As $L_2/\lambda_m > L_O/\lambda_m$, MS_c serves as the incident wave, resulting in a curved triple-point trajectory.

The experimental results validate the presence of all three modes, providing conclusive support for the curved Mach stem model. Figure 18(*a*) shows the typical records of mode 1. The early termination of the frozen limit at $L_2/\lambda_m = L_O/\lambda_m$ (i.e. $4\lambda_m$ for the wedge

https://doi.org/10.1017/jfm.2026.11751 Published online by Cambridge University Press

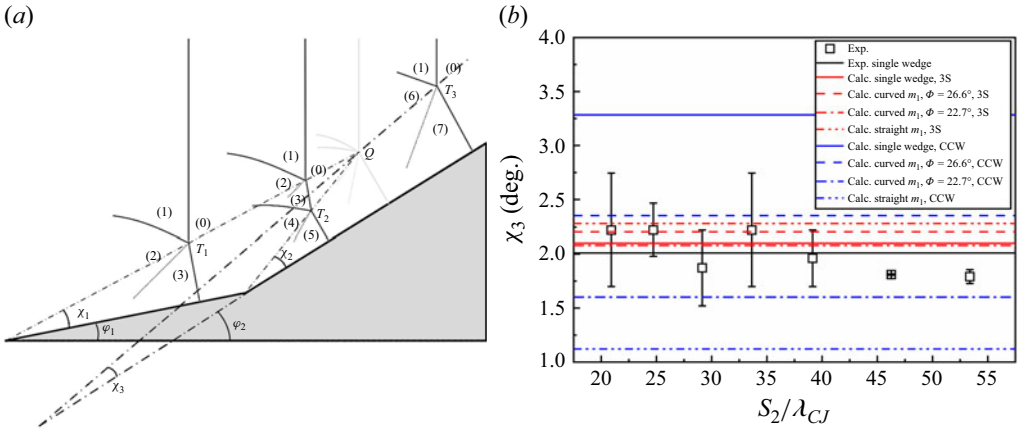


Figure 19. (*a*) Simplified model without considering the interaction between two triple points. (*b*) Asymptotic triple-point trajectory angle of MR3 for the case $\varphi_1 = 15°$, $\varphi_2 = 30°$.

B2) can be observed. As $L_2/\lambda_m > L_O/\lambda_m$, a curved triple-point trajectory influenced by MS_c occurs. Figures 18(*b*) and 18(*d*) show the typical records of mode 2. For the cases of mode 2, it is observed that the frozen limit exists within $L_2/\lambda_m = 5$. Within $5 < L_2/\lambda_m < L_O/\lambda_m$, the transition stage caused by MS_s can be observed. In the far field ($L_2/\lambda_m > 10$), the asymptotic triple-point trajectory angle is significantly smaller than the prediction of the reactive theories, which indicates the effect of MS_c. Figure 18(*c*) shows the typical records of mode 3. The localised self-similarity can be observed within $L_2/\lambda_m < L_O/\lambda_m$. For the triple-point trajectory within $10 < L_2/\lambda_m < L_O/\lambda_m$, the equilibrium limit caused by MS_s occurs, where the asymptotic trajectory angle is in good agreement with the prediction of the reactive theories. Meanwhile, it is noted that the trajectory angle predicted by the classical reactive theories is close to θ_2, and the trajectories in figure 18(*c*) are barely straight. Thus the premise that the trajectory of T_2 is straight before O is approximately valid for (4.10).

4.3. *The MR after the interaction between two triple points*

The second triple point T_2 will catch up with the first one T_1 at Q, then an interaction between them takes place. After the interaction, a new MR configuration (MR3) occurs. Ben-Dor *et al.* (1987) systematically investigated the reflections of planar shock waves on double wedges. They skipped the interaction between two triple points by simplification (see figure 19*a*). In the simplified frame, the wave structure after Q is a classical three-wave structure of MR. The Mach stem in MR3 is denoted as m_3 for the simplified frame. The detonation polar serves as an intuitive approach for investigating the MR of detonations (Bdzil & Short 2017). Without considering the interaction, the detonation polar is shown in figure 20, where Θ is the streamline turning angle behind the detonation wave. The states of the regions in figure 19*a* are represented by the corresponding points in figure 20. It can be found that the detonation polar of MR3 is only related to the state (1). Thus whether m_1 is curved or not will not influence the detonation polar of MR3. According to the detonation polar, when the interaction between two triple points is skipped, MR3 can be simplified to MR of a detonation wave over a single wedge. The experimental results indicate that with the travel of T_3, the asymptotic trajectory angle of MR3 (χ_3) trends to that obtained from a single wedge (see figure 19*b*). This finding proves that the simplified model is valid in the far field of MR3. However, it should be noted that there is a difference

https://doi.org/10.1017/jfm.2026.11751 Published online by Cambridge University Press

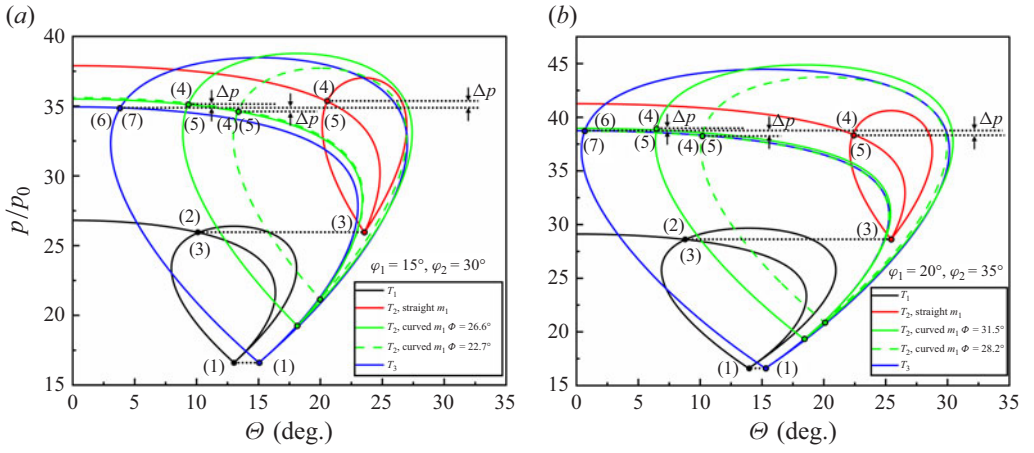


Figure 20. Detonation polar for the cases (*a*) $\varphi_1 = 15°$, $\varphi_2 = 30°$, (*b*) $\varphi_1 = 20°$, $\varphi_2 = 35°$.

(Δp) between the pressure behind the second Mach stem (p_5) and that behind the newly formed one (p_7). According to Ben-Dor *et al.* (1987), this difference can be considered to be dissipated in the flow field.

In the vicinity of Q, the interaction between T_1 and T_2 cannot be ignored. The existence of Δp indicates that there must be other disturbances generated at Q (Xie *et al.* 2005). Since the upward-travelling shock–shock is observed in many experiments, the additional disturbance generated at Q should be downward-travelling where m_2 serves as incident detonation wave (or undisturbed detonation wave). The downward-travelling disturbance can be either compressive (i.e. a shock–shock or a triple point) or expansive (i.e. a centred shock–expansion or expansion wave). The gas dynamic method and the shock dynamic method can be used for studying this problem. It should be noted that all the following analyses are based on the mixture parameters of $p_0 = 30$ kPa presented in table 2.

4.3.1. *Gas dynamic method (3S)*

For the gas dynamic method, the detonation polar is used to determine the property of the downward-travelling disturbance (see figure 20). The details of the detonation polar are presented in Appendix A. The downward-travelling disturbance is proposed to explain the existence of the pressure difference between two successive MRs on the double wedge, and a single MR on the second wedge surface, namely, $\Delta p = p_5 - p_7$ in figure 20. A new Mach stem m_2' is introduced due to the downward-travelling disturbance. If the unknown downward-travelling disturbance is a centred shock–expansion (see figure 21*a*), then there exist the relations

$$\varphi_2' > \varphi_2, \quad M_{m3} < M_{m2}' < M_{m2}, \tag{4.14}$$

where φ_2' is the equivalent wedge angle of a virtual wall surface, and M_{m2}', M_{m2}, M_{m3} are Mach numbers of m_2', m_2, m_3, respectively. Since $M_{m3} < M_{m2}$, Δp must be positive when a centred shock–expansion occurs. If the unknown downward-travelling disturbance is a shock–shock (see figure 21*b*), then there exist the relations

$$\varphi_2' < \varphi_2, \quad M_{m2} < M_{m2}' < M_{m3}. \tag{4.15}$$

Since $M_{m3} > M_{m2}$, Δp must be negative when a shock–shock occurs. As shown in figure 20(*a*), Δp is positive for the cases of straight m_1 and curved m_1 with $\Phi = 26.6°$;

https://doi.org/10.1017/jfm.2026.11751 Published online by Cambridge University Press

M_{m3}, exp.	M_{m3}, calc. by 3S	M_{m2} straight, calc. by 3S	M_{m2} $\Phi = 26.6°$	M_{m2} $\Phi = 22.7°$
5.925	5.930	5.956	5.944	5.921

Table 4. Mach numbers of m_2 and m_3 for the case $\varphi_1 = 15°$, $\varphi_2 = 30°$.

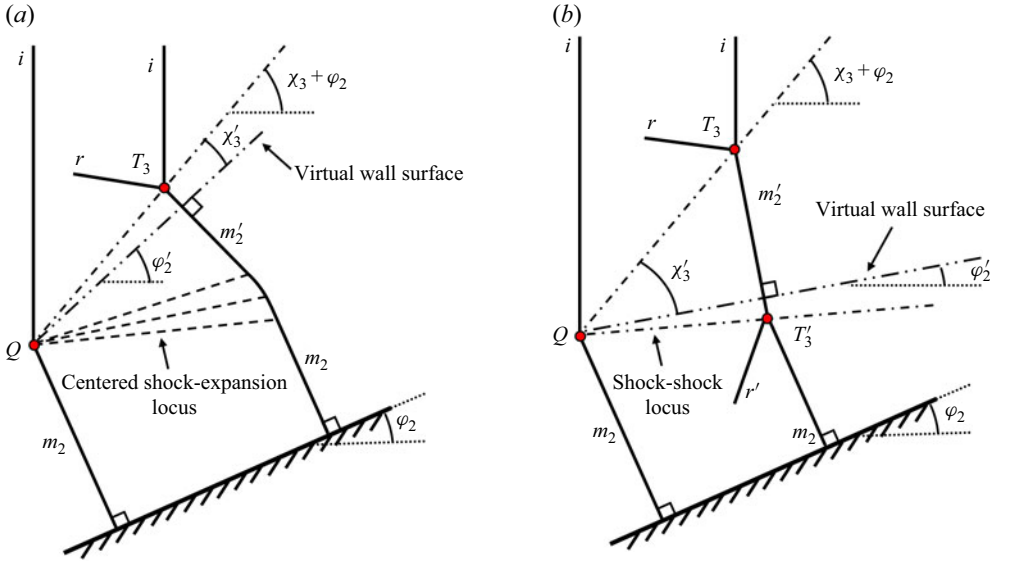


Figure 21. (*a*) Wave structure featuring a downward-travelling centred shock–expansion. (*b*) Wave structure featuring a downward-travelling shock–shock.

Φ is obtained from (4.12), representing the curvature degree of m_1. Thus the downward-travelling disturbance is a centred shock–expansion (or expansion wave). However, Δp is negative for the case of curved m_1 with $\Phi = 22.7°$. Thus the downward-travelling disturbance is a shock–shock (or a triple point). Table 4 shows the Mach numbers of Mach stems, from which the same conclusion can be drawn.

Figure 21(*a*) shows the wave structure featuring a downward-travelling centred shock–expansion, corresponding to the cases of straight m_1 and curved m_1 with $\Phi = 26.6°$. This model indicates that after the collision of two triple points, in addition to the newly-formed upward-travelling triple point, a downward-travelling expansive disturbance is also generated. A virtual wall surface is introduced, which is crossing Q and perpendicular to m_2'. The flow field can be precisely determined once the values of M_{m2}' and φ_2' are obtained. By introducing the virtual wall, this problem can be decomposed into an MR and a diffraction. For the MR, the relation between M_{m2}' and φ_2' can be obtained from (2.1):

$$M_{m2}' = F_{3S}(M_i, \varphi_2'). \tag{4.16}$$

For the detonation diffraction, the downward-travelling disturbance is a simple wave. According to the simple wave relation, we have

$$\varphi_2' - \varphi_2 = -\int_{M_{m2}}^{M_{m2}'} \frac{1}{A(M)\, c(M)}\, \mathrm{d}M, \tag{4.17}$$

https://doi.org/10.1017/jfm.2026.11751 Published online by Cambridge University Press

where $A(M)$ and $c(M)$ refer to (4.7) and (4.8), respectively. The values of M'_{m2} and φ'_2 can be obtained from the system consisting of (4.16) and (4.17), where M_i, M_{m2}, φ_2 are known. There are two unknown variables, M'_{m2} and φ'_2, so the equations are closed. For the case of curved m_1, M_{m2} can be obtained from (4.18*a*) below, and for the case of straight m_1, M_{m2} can be obtained from (4.18*b*):

$$M_{m2} = F_{3S}(\overline{\alpha} M_i, \Phi), \quad M_{m2} = F_{3S}(M_{m1}, \Delta\varphi), \tag{4.18a,b}$$

where Φ and $\overline{\alpha}$ can be obtained from (4.12) and (4.13), respectively.

Figure 21(*b*) shows the wave structure featuring a downward-travelling shock–shock, corresponding to the case of curved m_1 with $\Phi = 22.7°$. This model indicates that after the collision of two triple points, in addition to the newly formed upward-travelling triple point, a downward-travelling triple point T'_3 is generated. By introducing the virtual wall, this problem can be decomposed into two MRs. Thus the values of M'_{m2} and φ'_2 can be obtained from the system

$$\left.\begin{aligned} M'_{m2} &= F_{3S}(M_i, \varphi'_2), \\ M'_{m2} &= F_{3S}(M_{m2}, \varphi_2 - \varphi'_2), \end{aligned}\right\} \tag{4.19}$$

where M_i, M_{m2}, φ_2 are known; M_{m2} can be obtained from (4.18). There are two unknown variables: M'_{m2} and φ'_2, so the equations are closed.

With the values of M'_{m2} and φ'_2 determined, χ_3 considering the interaction between T_1 and T_2 can be calculated by

$$\chi_3 = \chi'_3 + \varphi'_2 - \varphi_2, \tag{4.20}$$

where χ'_3 is the asymptotic triple-point trajectory angle over the virtual wall. According to (2.6), χ'_3 can be obtained from

$$M'_{m2} = M_i \cos\chi'_3 / \cos(\chi'_3 + \varphi'_2). \tag{4.21}$$

Figure 19(*b*) shows χ_3 considering the interaction between T_1 and T_2. In general, the theoretical results using the gas dynamic method indicate that the interaction between T_1 and T_2 has a tiny impact on χ_3 for the case $\varphi_1 = 15°$, $\varphi_2 = 30°$. The downward-travelling shock–shock disturbance leads to a reduction in χ_3 compared to that over a single wedge. In contrast, the downward-travelling centred shock–expansion disturbance shows the opposite effect.

Figure 20(*b*) shows the detonation polar for the case $\varphi_1 = 20°$, $\varphi_2 = 35°$; Δp is positive for the case of curved m_1 with $\Phi = 31.5°$. Thus the downward-travelling disturbance is a centred shock–expansion. On the contrary, Δp is negative for the cases of straight m_1 and curved m_1 with $\Phi = 28.2°$. Thus the downward-travelling disturbance is a shock–shock. Table 5 shows the Mach numbers of the Mach stems. Because of the limitation of the reactive 3S theory when $\varphi_1 > 30°$ (see figure 6*b*), M_{m3} obtained from experiment is significantly larger than that calculated by the reactive 3S theory. The experimental result indicates that for the case of curved m_1 with $\Phi = 31.5°$, the downward-travelling disturbance should be a shock–shock, which is inconsistent with the result obtained from the detonation polar.

4.3.2. *Shock dynamic method (CCW)*

For the shock dynamic method, a shock–shock polar $((M_w/M_u) - \delta)$, based on the shock–shock relation (2.2), is used to determine the property of the downward-travelling disturbance. Figure 22 shows the shock–shock polar. For the unification of coordinates, the vertical axis is M_w/M_i, and δ of i is 0. According to (2.2), for a certain incident

https://doi.org/10.1017/jfm.2026.11751 Published online by Cambridge University Press

M_{m3}, exp.	M_{m3}, calc. by 3S	M_{m2} straight, calc. by 3S	M_{m2} $\Phi = 31.5°$	M_{m2} $\Phi = 28.2°$
6.231	6.159	6.140	6.163	6.133

Table 5. Mach numbers of m_2 and m_3 for the case $\varphi_1 = 20°$, $\varphi_2 = 35°$.

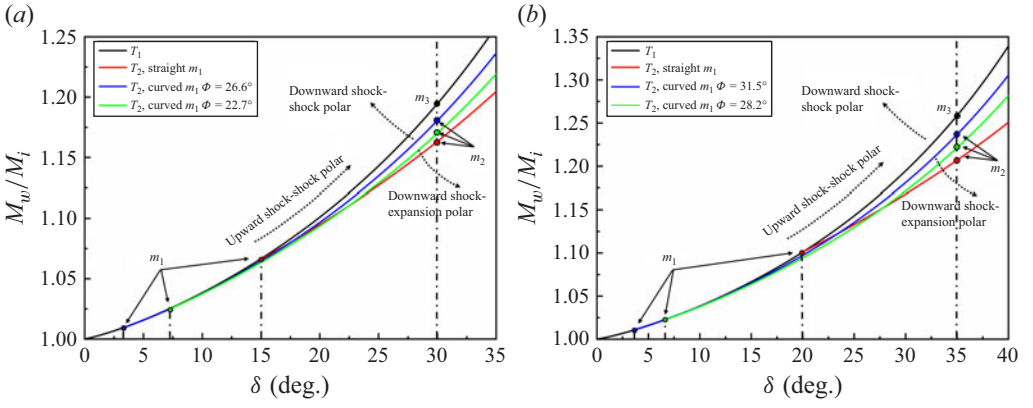


Figure 22. Shock–shock polar for the cases (*a*) $\varphi_1 = 15°$, $\varphi_2 = 30°$, (*b*) $\varphi_1 = 20°$, $\varphi_2 = 35°$.

detonation (i.e. a certain M_u), the state point (δ, M_w) must be on the corresponding shock–shock polar. For MR1, the incident detonation is i and $M_u = M_i$. For MR2, the incident detonation is m_1 and $M_u = M_{m1}$. Since $M_i \neq M_{m1}$ and $M_{m1\text{-}straight} \neq M_{m1\text{-}curved}$, the corresponding shock–shock polars deviate from each other. Since the incident detonation is also i, the state point representing m_2' must be on the upward shock–shock polar of MR1. If the unknown downward-travelling disturbance is a centred shock–expansion (see figure 21*a*), then there exist the relations

$$\varphi_2' > \varphi_2, \quad M_{m3} < M_{m2}' < M_{m2}. \tag{4.22}$$

Thus the downward shock–expansion polar starting from the state point of m_2' must extend to the lower right. As shown in figure 22, for the cases $\varphi_1 = 15°$ and $\varphi_1 = 20°$, the shock–expansion polar will not cross the shock–shock polar of MR1. This means thaty there is no solution if a centred shock–expansion is generated at Q. If the unknown downward-travelling disturbance is a shock–shock (see figure 21*b*), then there exist the relations

$$\varphi_2' < \varphi_2, \quad M_{m2} < M_{m2}' < M_{m3}. \tag{4.23}$$

Thus the downward shock–shock polar starting from the point of m_2' must extend to the upper left. As shown in figure 22, for the cases $\varphi_1 = 15°$ and $\varphi_1 = 20°$, the downward-travelling shock–shock polar will cross the shock–shock polar of MR1. Thus the downward-travelling disturbance generated at Q is a shock–shock.

For the case of the downward-travelling shock–shock disturbance (see figure 21*b*), the values of M_{m2}' and φ_2' can be obtained from the equation system

$$\left.\begin{aligned} \varphi_2' &= F_{S\text{-}S}(M_i, M_{m2}'), \\ \varphi_2 - \varphi_2' &= F_{S\text{-}S}(M_{m2}, M_{m2}'), \\ \Phi &= F_{S\text{-}S}(\overline{\alpha} M_i, M_{m2}), \end{aligned}\right\} \tag{4.24}$$

https://doi.org/10.1017/jfm.2026.11751 Published online by Cambridge University Press

where φ_2 and M_i are known, and Φ and $\overline{\alpha}$ can be obtained from (4.12) and (4.13), respectively. There are three unknown variables, M'_{m2}, φ'_2 and M_{m2}, so the equations are closed. With the values of M'_{m2} and φ'_2 determined, χ_3 considering the interaction between T_1 and T_2 can be calculated by (4.20). As shown in figure 19(b), the theoretical results indicate a significant reduction in χ_3 resulting from the downward-travelling shock–shock disturbance.

For the case of the downward-travelling centred shock–expansion (see figure 21a), the values of M'_{m2} and φ'_2 can be obtained from the equation system

$$\left.\begin{aligned} &\varphi'_2 = F_{S\text{-}S}\left(M_i,\, M'_{m2}\right),\\ &\varphi'_2 - \varphi_2 = -\int_{M_{m2}}^{M'_{m2}} \frac{1}{A(M)\,c(M)}\,\mathrm{d}M,\\ &\Phi = F_{S\text{-}S}\left(\overline{\alpha} M_i,\, M_{m2}\right). \end{aligned}\right\} \tag{4.25}$$

4.3.3. *Discussions on the two methods*

The downward-travelling disturbance is essentially determined by the relation between M_{m2} and M_{m3}. When $M_{m3} > M_{m2}$, the downward-travelling disturbance is a shock–shock. When $M_{m3} < M_{m2}$, a centred shock–expansion occurs. The gas dynamic method and the shock dynamic method are based on the reactive 3S theory and the reactive CCW theory, respectively. In § 4.3.2, the gas dynamic method indicates the occurrence of a centred shock–expansion for the cases $\varphi_1 = 15°$, $\varphi_2 = 30°$ straight m_1 and curved m_1 with $\Phi = 26.6°$. However, for the same cases, a shock–shock can be determined by the shock dynamic method. In fact, the wave structure after Q is essentially determined by the strength of the Mach stems m_2 and m_3 – namely, by the pressures p_5 and p_7 (see figure 20), or by their corresponding Mach numbers M_{m2} and M_{m3}. Both methods give a relatively accurate prediction for φ_1 used in this study (i.e. $\varphi_1 = 15°$, $20°$, $25°$). Thus the main factor causing the deviation between the two methods is the prediction accuracy in φ_2 (see figure 6b). As shown in figure 19(b), for the case $\varphi_1 = 15°$, $\varphi_2 = 30°$, χ_3 calculated by the reactive CCW theory is significantly larger than the experimental result, while the prediction of the 3S theory is consistent with the experimental result. Thus the gas dynamic method is more appropriate for the case $\varphi_1 = 15°$, $\varphi_2 = 30°$. As for $\varphi_1 = 20°$, $\varphi_2 = 35°$, on the contrary, the actual wave structure should approximate that predicted by the reactive CCW theory (see figure 23). In general, the gas dynamic method and the shock dynamic method should be combined to determine the wave structure and the parameters subsequent to the interaction between two triple points. It should be noted that the reactive 3S theory and the reactive CCW theory are unsolvable as the wedge angle is larger than the critical angle. As shown in figure 6(b), the reactive 3S theory underestimates the critical wedge angle, which was found to be approximately 50° by Li *et al.* (2018). Thus when φ_2 is larger than the theoretical critical wedge angle, the theoretical models have no solutions. Despite all the discrepancies among the theories, a qualitative conclusion can be drawn as follows. The downward-travelling shock–shock disturbance caused by the interaction between two triple points will result in a reduction in χ_3 compared to that over a single wedge (see figure 19b). In contrast, the downward-travelling centred shock–expansion disturbance shows the opposite effect.

In § 4.2, a curved Mach stem m_1 is introduced. The curved Mach stem m_1 leads to the variation of χ_2 (see figure 16), which consequently results in the variation of M_{m2}. Since the value of M_{m3} is close to M_{m2} for some cases, e.g. $\varphi_1 = 15°$, $\varphi_2 = 30°$ (see figure 23), the variation of the Mach stem curvature can lead to different wave structures. For the

https://doi.org/10.1017/jfm.2026.11751 Published online by Cambridge University Press

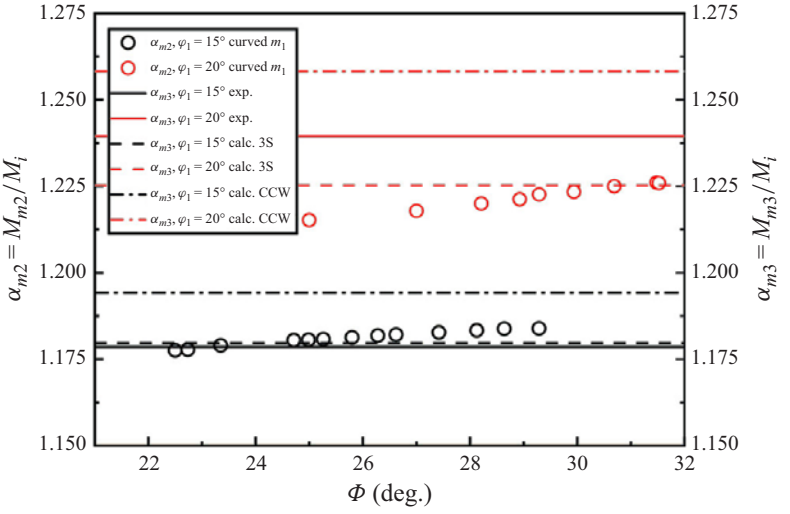


Figure 23. Overdrive degree of the Mach stem m_2 against the equivalent wedge angle.

case $\varphi_1 = 15°$, $\varphi_2 = 30°$, the downward-travelling disturbance changes from a shock–shock ($M_{m3} > M_{m2}$) to a shock–expansion ($M_{m3} < M_{m2}$) as Φ increases. The classical straight Mach stem assumption indicates a fixed value of M_{m2} for certain φ_1 and φ_2, which consequently leads to a certain wave structure. Thus the assumption of a straight Mach stem m_1 will lead to a misjudgement of the wave structure.

5. Conclusion

In this paper, the MR of a detonation wave over a concave double wedge was investigated experimentally and theoretically. The experimental results indicate that the classic reactive theories based on the straight Mach stem assumption cannot accurately predict the behaviours of MRs on the second wedge surface. The effects of a curved Mach stem m_1 on the last two MRs are emphasised. A theoretical model is proposed to predict the MR behaviour over a concave double wedge.

Over the second wedge surface, the MR of an overdriven detonation wave was observed. A curved Mach stem model was constructed, which introduces a straight Mach stem (MS_s) perpendicular to the wedge surface, a concave curved Mach stem (MS_c) near the triple point, and a point P defined as the boundary between MS_s and MS_c. The trajectory of P is a straight line in the equilibrium limit, whose slope is only related to the wedge angle. The concave curvature of MS_c implies a lower overdrive degree and a smaller incident angle, which consequently leads to a smaller χ_2 than the prediction of the classical theories. Based on the curved Mach stem model, an equivalent wedge angle Φ and an equivalent overdrive degree $\overline{\alpha}$ can be applicable to predict the value of χ_2. Three localised self-similarity modes induced by the curved Mach stem model are experimentally proved. (i) Mode 1 ($L_O/\lambda_m < 5$): the frozen limit terminates prematurely at $L_2/\lambda_m = L_O/\lambda_m$. (ii) Mode 2 ($5 < L_O/\lambda_m < 10$): a complete frozen limit occurs within $L_2/\lambda_m < 5$. (iii) Mode 3 ($L_O/\lambda_m > 10$): within $L_2/\lambda_m < L_O/\lambda_m$, a complete MR process of a planar overdriven detonation can be observed, which possesses both the frozen and equilibrium limits. The classical reactive theory is applicable to the MR process of planar overdriven detonations.

An analytical model was developed and solved to analyse the interaction of two triple points that can be formed over concave double wedges. The collision of the second triple

https://doi.org/10.1017/jfm.2026.11751 Published online by Cambridge University Press

point T_2 with the first one T_1 at point Q leads to an upward-travelling shock–shock and an unknown downward-travelling disturbance. The gas dynamic method and the shock dynamic method are applied to determine the unknown downward-travelling disturbance. For both methods, the unknown downward-travelling disturbance is essentially determined by the relation between M_{m2} and M_{m3}. When $M_{m3} > M_{m2}$, the downward-travelling disturbance is a shock–shock. When $M_{m3} < M_{m2}$, a centred shock–expansion occurs. By introducing a virtual wall, the entire flow field can be solved using the gas dynamic method and the shock dynamic method. The downward-travelling shock–shock disturbance will result in a reduction in χ_3 compared to that over a single wedge. The downward-travelling centred shock–expansion disturbance presents the opposite effect. The curved Mach stem m_1 leads to the variation of M_{m2}, which further results in the variation of the wave structure.

The above results imply that the present curved Mach stem model is valid for the MR of a detonation wave over a concave double wedge. Meanwhile, the present study indicates that when one aims to obtain a planar overdriven detonation wave through the MR, the existence of MS_c must be taken into account. It is believed that the present study can be used to better understand the phenomena of detonation reflections over complex structures such as double wedges. However, the limitations of the classical theories for a large wedge angle (e.g. $\varphi > 30°$) are still unresolved in the present study. The results of the present study are limited to the mixture $2\mathrm{H}_2 + \mathrm{O}_2 + 2\mathrm{Ar}$. Therefore, further experiments should be carried out using a variety of gas mixtures for varying the instability.

Supplementary materials. Supplementary materials are available at https://doi.org/10.1017/jfm.2026.11751.

Funding. This work was supported by the National Natural Science Foundation of China under project nos 12272374 and 12472373, and the Collaborative Innovation Programme of Hefei Science Centre, CAS (no. 2022HSC-CIP027).

Declaration of interests. The authors report no conflict of interest.

Author contributions. Z.-Y.Z.: writing – original draft, investigation, fata curation. H.-H.M.: writing – review & editing, supervision. L.-Q.W.: writing – review & editing, validation, conceptualisation.

Appendix A. Reactive 3S theory for MR of detonation waves

Based on the oblique detonation wave relations (Li *et al.* 1997), a solution procedure of the reactive 3S theory is presented as follows. The reactive 3S theory assumes that the Mach stem m is straight and normal to the wedge surface, and that the triple point T propagates along a straight line emanating from the leading edge of the reflecting wedge. Thus the problem is, in fact, pseudo-steady. When the coordinate system is fixed at T, the problem turns into a steady one. Figure 24(a) illustrates the wave configuration of an MR. The incident wave i and the Mach stem m are detonation waves; the reflected wave r is a shock wave. The pressure of state (0) (p_0), Mach number of the incident wave M_i and wedge angle φ are known. Additionally, for a certain initial pressure, M_{CJ}, γ_0, γ_1 can be obtained via the Shock and Detonation Toolbox (EDL 2023) in Cantera (Goodwin 2003) with the GRI30 detailed chemical mechanism. The triple-point trajectory angle χ and Mach number of the Mach stem M_m need to be solved.

Since the Mach stem is straight and the triple point propagates along a straight line, the following geometrical relations can be obtained:

$$\phi_1 = \frac{\pi}{2} - (\varphi + \chi), \tag{A1}$$

$$\phi_3 = \frac{\pi}{2} - \chi, \tag{A2}$$

https://doi.org/10.1017/jfm.2026.11751 Published online by Cambridge University Press

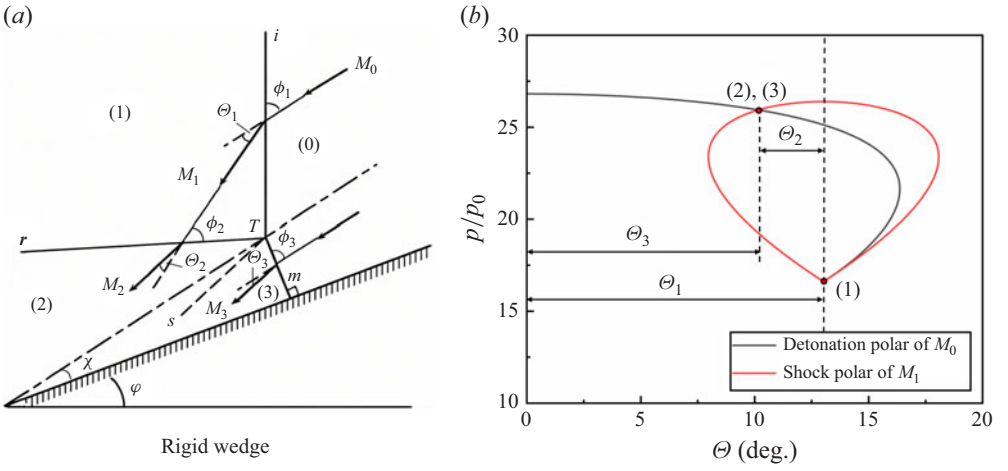


Figure 24. (*a*) Schematic illustration of the wave configuration of an MR and definition of the flow parameters. (*b*) Detonation polar for the case $\varphi = 15°$.

where ϕ_1 and ϕ_3 are the angles of incidence. In addition, the pseudo-steady flow Mach number in state (0) (M_0) can be obtained from

$$M_0 = \frac{M_i}{\sin\phi_1}. \tag{A3}$$

According to the oblique detonation wave relations (Li *et al.* 1997), the pressures of state (1) (p_1) and state (3) (p_3) can be obtained from

$$p_1 = p_0 \frac{(1+\sigma_1)\gamma_0 M_0^2 \sin^2\phi_1 - \gamma_1\sigma_1 + 1}{\gamma_1 + 1}, \tag{A4}$$

$$p_3 = p_0 \frac{(1+\sigma_3)\gamma_0 M_0^2 \sin^2\phi_3 - \gamma_1\sigma_3 + 1}{\gamma_1 + 1}, \tag{A5}$$

where

$$\sigma_1 = \left[1 - \frac{2\left(\gamma_1^2 - 1\right)M_0^2 \sin^2\phi_1\,(\overline{q} + \eta)}{\left(M_0^2 \sin^2\phi_1 - (\gamma_1/\gamma_0)\right)^2}\right]^{1/2}, \tag{A6}$$

$$\sigma_3 = \left[1 - \frac{2\left(\gamma_1^2 - 1\right)M_0^2 \sin^2\phi_3\,(\overline{q} + \eta)}{\left(M_0^2 \sin^2\phi_3 - (\gamma_1/\gamma_0)\right)^2}\right]^{1/2}, \tag{A7}$$

$$\eta = \frac{\gamma_1 - \gamma_0}{\gamma_0(\gamma_0 - 1)(\gamma_1 - 1)}, \tag{A8}$$

$$\overline{q} = \frac{\gamma_1^2(\gamma_0 - 1) + 2\gamma_0\left(\gamma_0 - \gamma_1^2\right)M_{CJ}^2 + \gamma_0^2(\gamma_0 - 1)M_{CJ}^4}{2\gamma_0^2(\gamma_0 - 1)(\gamma_1^2 - 1)M_{CJ}^2}. \tag{A9}$$

The deflection angles of the flows Θ_1 and Θ_3 can be obtained from

$$\Theta_1 = \phi_1 - \arctan\left[\frac{\gamma_1 - \sigma_1}{\gamma_1 + 1}\tan\phi_1 + \frac{2\gamma_1(1+\sigma_1)}{\gamma_0(\gamma_1+1)M_0^2 \sin 2\phi_1}\right], \tag{A10}$$

$$\Theta_3 = \phi_3 - \arctan\left[\frac{\gamma_1 - \sigma_3}{\gamma_1 + 1}\tan\phi_3 + \frac{2\gamma_1(1+\sigma_3)}{\gamma_0(\gamma_1+1)M_0^2 \sin 2\phi_3}\right]. \tag{A11}$$

https://doi.org/10.1017/jfm.2026.11751 Published online by Cambridge University Press

The flow Mach number in state (1) (M_1) can be obtained from $M_1 = V_1/a_1 = (M_0 \cos\phi_1/\cos(\phi_1 - \Theta_1))(a_0/a_1)$, where V_1 is the flow velocity of state (1), and a_0 and a_1 are the sonic velocities of states (0) and (1) respectively. Here, a_0/a_1 can be obtained from the oblique detonation wave relations (Li *et al.* 1997). Thus M_1 can be expressed as

$$M_1 = \frac{M_0 \cos\phi_1}{\cos(\phi_1 - \Theta_1)} \times \frac{(\gamma_1 + 1) M_0 \sin\phi_1}{\left\{(1+\sigma_1)\gamma_1 M_0^2 \sin^2\phi_1 - \left[\gamma_1(\gamma_1\sigma_1 - 1)/\gamma_0\right]\right\}^{1/2} \left\{(\gamma_1 - \sigma_1) M_0^2 \sin^2\phi_1 + \left[\gamma_1(1+\sigma_1)/\gamma_0\right]\right\}^{1/2}}. \tag{A12}$$

According to the oblique shock wave relations (Ben-Dor 2007), the pressure p_2 and deflection angle Θ_2 of state (2) can be obtained from

$$p_2 = p_1 \frac{2}{\gamma_1 + 1}[\gamma_1 M_1^2 \sin^2\phi_2 - (\gamma_1 - 1)/2], \tag{A13}$$

$$\Theta_2 = \arctan\left[2\cot\phi_2 \frac{M_1^2 \sin^2\phi_2 - 1}{M_1^2(\gamma_1 + \cos 2\phi_2) + 2}\right]. \tag{A14}$$

The matching conditions across the slipstream s are

$$\Theta_1 \mp \Theta_2 = \Theta_3 \tag{A15}$$

and

$$p_2 = p_3. \tag{A16}$$

This set of 12 equations, namely, (A1)–(A5) and (A10)–(A16), contains 12 unknowns: ϕ_1, ϕ_2, ϕ_3, p_1, p_2, p_3, Θ_1, Θ_2, Θ_3, M_0, M_1 and χ. Consequently, the set is complete and can, in principle, be solved. The Mach number of the Mach stem M_m can be expressed by

$$M_m = M_i \cos\chi / \cos(\chi + \varphi). \tag{A17}$$

For a certain mixture, χ is a function of M_i and φ (i.e. $\chi(M_i, \varphi)$). Thus (A17) can be rewritten as the following function for convenience:

$$M_m = F_{3S}(M_i, \varphi). \tag{A18}$$

It is rather difficult to solve the system (A1)–(A5) and (A10)–(A16) directly. Alternatively, the detonation polar ($(p/p_0) - \Theta$) can be utilised to solve the problem (see figure 24*b*). Once the flow Mach number M ahead of the detonation front is fixed, a specific detonation polar corresponding to M can be determined. As shown in figure 24(*a*), M_0 is the flow Mach number ahead of i and m, which means that the points representing states (1) and (3) lie on the same detonation polar of M_0. The detonation polar of M_0 can be obtained from (A4) and (A10). The reflected wave r is a non-reactive shock wave, for which the shock polar can be derived from (A13) and (A14). The point of state (2) lies on the shock polar of M_1. Considering the matching conditions across the slipstream s ((A15) and (A16)), the points of states (2) and (3) should be the intersection of the detonation polar and the shock polar.

Appendix B. Typical soot foil records and detection of cellular characteristics

The soot foil records were digitised using a camera or a scanner. Figures 25, 26 and 27 illustrate the typical soot foil records for different double wedges and p_0 (for original

https://doi.org/10.1017/jfm.2026.11751 Published online by Cambridge University Press

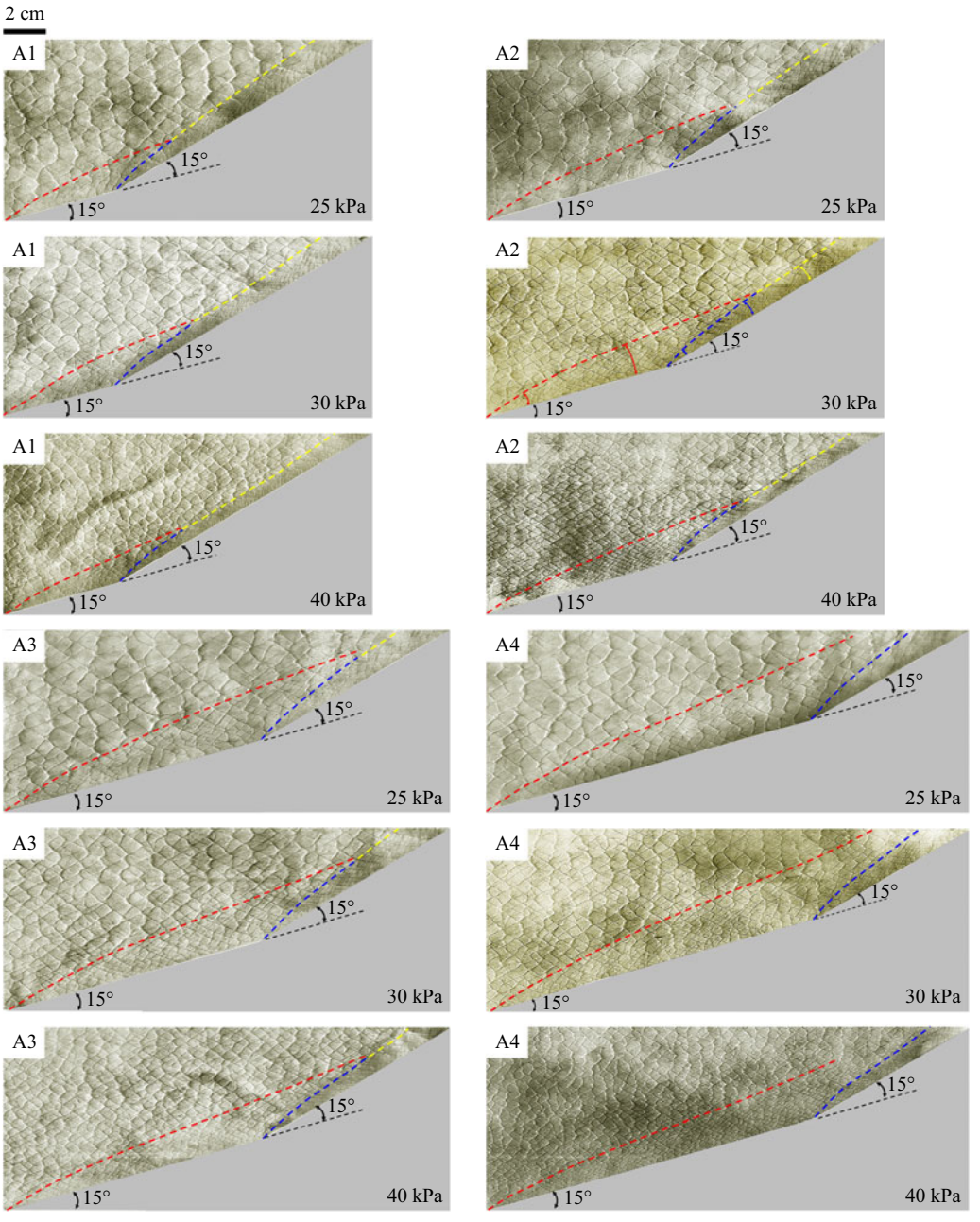


Figure 25. Typical soot foil records of wedges A1–A4.

figures, see the supplementary material are available at https://doi.org/10.1017/jfm.2026.11751). Figure 28 presents a procedure for detecting cellular characteristics from a soot foil sample. First, a square region (or other shapes, as long as they contain enough cells) was selected from the soot foil. Within this image, the intersections of cell boundary trajectories could be identified, and the corresponding coordinates were recorded. Then the cell size and shape could be obtained using the coordinates. Detonation in the

https://doi.org/10.1017/jfm.2026.11751 Published online by Cambridge University Press

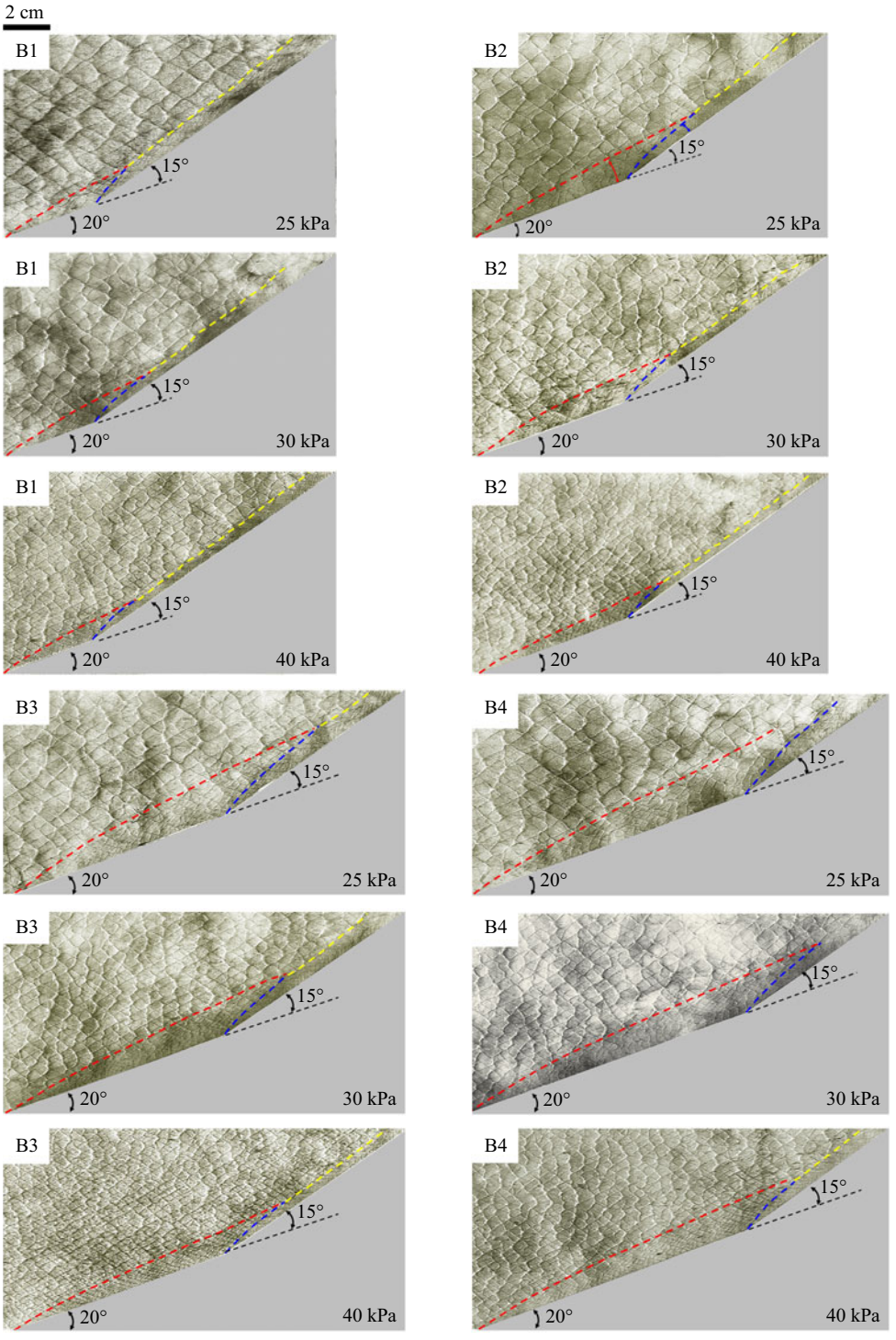


Figure 26. Typical soot foil records of wedges B1–B4.

https://doi.org/10.1017/jfm.2026.11751 Published online by Cambridge University Press

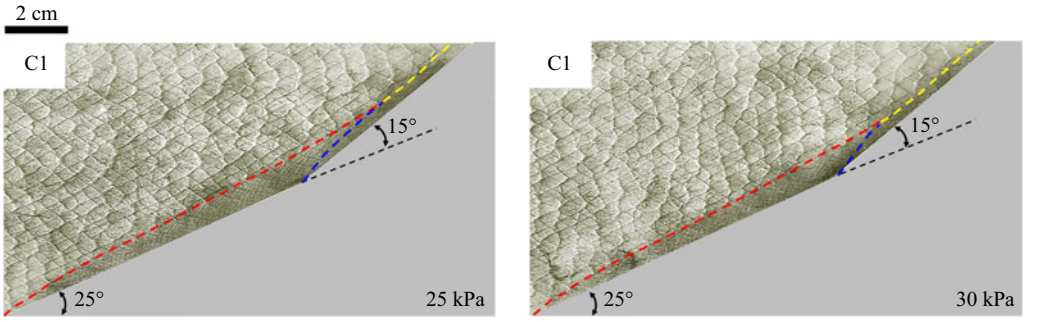


Figure 27. Typical soot foil records of wedge C1.

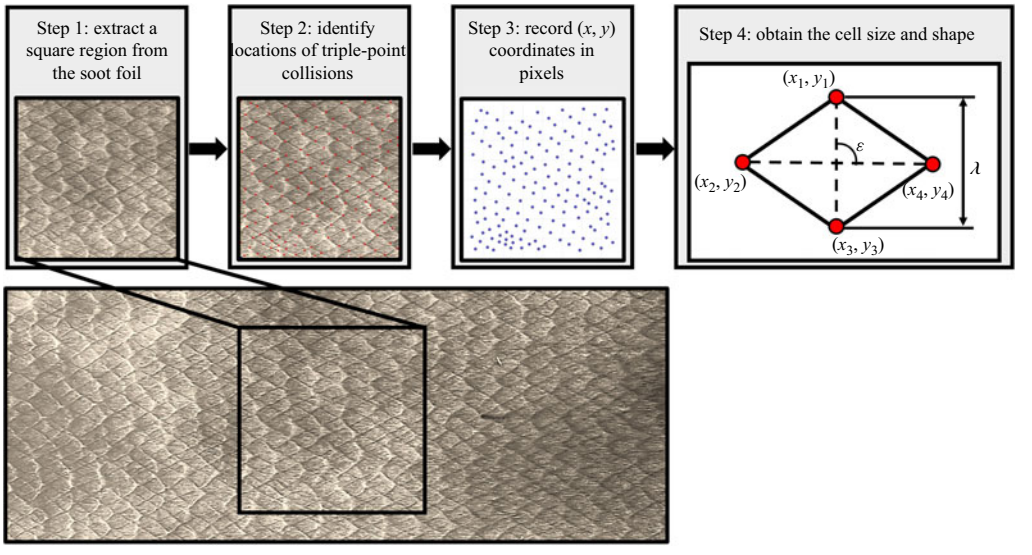


Figure 28. A procedure for detecting cellular characteristics from a soot foil sample. Here, λ is cell size, and ε is characteristic angle.

mixture $2H_2 + O_2 + 2Ar$ is categorised as stable with regular cellular structure (Ng & Zhang 2011), which is convenient for measuring cell size and determining the triple-point trajectory.

The determination of the triple-point trajectory through the soot foil is widely proved by numerous studies (Akbar 1971; Fortin *et al.* 2015; Li *et al.* 2018; Chen *et al.* 2023; Ji, Ma & Wang 2023; Zhou *et al.* 2024). Generally, a triple-point trajectory can be found by examining the change in cell size and shape. Since the Mach stem is essentially an overdriven detonation, the cell size is significantly smaller than that of the cells behind the incident wave. A quantitative analysis of cell size is provided in § 4.1 (see figure 5*b*). Furthermore, the cell shape also changes. A quantitative analysis of cell shape is provided in § 4.2.1 (see figure 8). By comparing these distinct differences, the triple-point trajectory can be obtained accordingly. According to Li *et al.* (2018), the downward trajectory of a natural transverse wave will bend anticlockwise when entering the Mach stem region. Thus by connecting these bending points, the boundary between the incident detonation region and the overdriven Mach stem region can also be determined.

https://doi.org/10.1017/jfm.2026.11751 Published online by Cambridge University Press

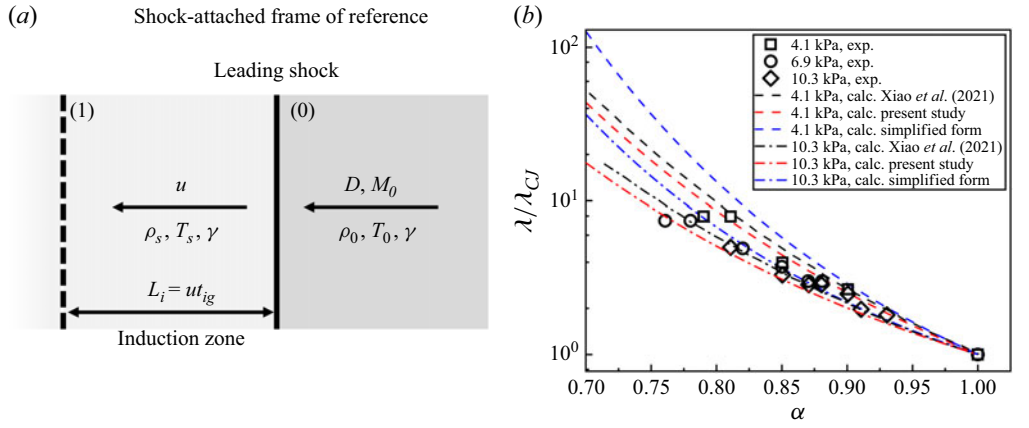


Figure 29. (*a*) Schematic illustration of the detonation wave structure with induction zone. (*b*) The relation between cell size λ and overdrive degree α, where $\alpha < 1$. The experimental results in (*b*) are obtained from Xiao *et al.* (2021). In (*b*), initial pressures 4.1 and 10.3 kPa correspond to $E_a/RT_{s,CJ} = 5.0$ and $E_a/RT_{s,CJ} = 3.8$, respectively.

Appendix C. Relationship between λ and α

Figure 29(*a*) presents a schematic illustration of the detonation wave structure in the shock-attached frame of reference. The parameters are defined as follows: L_i is the induction zone length; t_{ig} is the chemical induction time; D, M_0, ρ_0, T_0, γ_0 respectively represent the flow velocity, flow Mach number, density, temperature and specific heat ratio before the leading shock (region (0)); u, ρ_s, T_s, γ_s respectively represent the flow velocity, density, temperature and specific heat ratio in the induction zone (region (1)). In the induction zone behind the leading shock, the flow can be regarded as that behind a non-reactive shock wave. The 1γ model is applied, i.e. $\gamma_0 = \gamma_s = \gamma$.

Since the ratio of the cell size to the chemical induction zone length remains constant when the overdrive degree changes (Huang & Xu 1987), the cell size λ behind the detonation wave with overdrive degree $\alpha = M_0/M_{CJ}$ can be expressed as

$$\frac{\lambda}{\lambda_{CJ}} \approx \frac{L_i}{L_{i,CJ}} = \frac{u}{u_{CJ}} \frac{t_{ig}}{t_{ig,CJ}}, \tag{C1}$$

where the subscript CJ represents the CJ detonation wave. Using the normal shock wave relations, the ratio u/u_{CJ} can be expressed by α and M_{CJ}:

$$\frac{u}{u_{CJ}} = \frac{D}{D_{CJ}} \frac{\rho_0}{\rho_s} \frac{\rho_{s,CJ}}{\rho_{0,CJ}} = \alpha^{-1} \frac{2 + (\gamma - 1)M_0^2}{2 + (\gamma - 1)M_{CJ}^2}. \tag{C2}$$

The simple formulation of t_{ig} is expressed as (Soloukhin & Ragland 1969)

$$t_{ig} = K\rho_s^{-n} \exp(E_a/RT_s), \tag{C3}$$

where K is the kinetic rate factor, E_a/RT_s is the normalised activation energy, and n is a constant depending on the reactive mixture ($n = 1$ generally). Considering $n = 1$, the ratio $t_{ig}/t_{ig,CJ}$ can be expressed as

$$\frac{t_{ig}}{t_{ig,CJ}} = \alpha^{-2} \frac{2 + (\gamma - 1)M_0^2}{2 + (\gamma - 1)M_{CJ}^2} \exp\left[\frac{E_a}{RT_{s,CJ}} \left(\frac{T_{s,CJ}}{T_s} - 1\right)\right]. \tag{C4}$$

https://doi.org/10.1017/jfm.2026.11751 Published online by Cambridge University Press

Using the normal shock wave relations, the ratio $T_{s,CJ}/T_s$ can be expressed as

$$\frac{T_{s,CJ}}{T_s}=\frac{T_{s,CJ}}{T_0}\frac{T_0}{T_s}=\alpha^2\frac{\left[2\gamma M_{CJ}^2-(\gamma-1)\right]\left[2+(\gamma-1)M_{CJ}^2\right]}{\left[2\gamma M_0^2-(\gamma-1)\right]\left[2+(\gamma-1)M_0^2\right]}. \tag{C5}$$

According to (C1)–(C5), the ratio λ/λ_{CJ} can be expressed as

$$\frac{\lambda}{\lambda_{CJ}}\approx\alpha^{-3}\left[\frac{2+(\gamma-1)M_0^2}{2+(\gamma-1)M_{CJ}^2}\right]^2 \times\exp\left[\frac{E_a}{RT_{s,CJ}}\left(\alpha^2\frac{\left[2\gamma M_{CJ}^2-(\gamma-1)\right]\left[2+(\gamma-1)M_{CJ}^2\right]}{\left[2\gamma M_0^2-(\gamma-1)\right]\left[2+(\gamma-1)M_0^2\right]}-1\right)\right]. \tag{C6}$$

For $2H_2+O_2+2Ar$ detonation waves, M_{CJ} approaches 5, and γ is 1.478 (see table 2). Considering that $2\gamma M_{CJ}^2\gg\gamma-1$, (C6) can be rewritten as

$$\frac{\lambda}{\lambda_{CJ}}\approx\frac{\beta^2}{\alpha^3}\exp\left[\frac{E_a}{RT_{s,CJ}}\left(\beta^{-1}-1\right)\right], \tag{C7}$$

$$\beta=\frac{2M_{CJ}^{-2}+(\gamma-1)\alpha^2}{2M_{CJ}^{-2}+(\gamma-1)}, \tag{C8}$$

where $E_a/RT_{s,CJ}$ can be calculated based on a procedure proposed by Ng (2005), and M_{CJ} and γ can be obtained via the Shock and Detonation Toolbox in Cantera. With a large M_{CJ} ($2M_{CJ}^{-2}\ll\gamma-1$ and $2M_{CJ}^{-2}\ll(\gamma-1)\alpha^2$), (C8) can be further simplified to

$$\frac{\lambda}{\lambda_{CJ}}\approx\alpha\exp\left[\frac{E_a}{RT_{s,CJ}}\left(\alpha^{-2}-1\right)\right]. \tag{C9}$$

The results in figure 5(*b*) indicate that for $\alpha>1$, the relation between λ/λ_{CJ} and α can be well predicted by (C7). Figure 29(*b*) shows the relation between λ and α, where $\alpha<1$. For $\alpha<1$, the results predicted by (C7) are well consistent with the experimental results obtained from Xiao *et al.* (2021). However, as α decreases, the results predicted by (C9) are not in agreement with the experimental results.

References

Akbar, R. 1971 Mach reflection of gaseous detonation. School PhD thesis, Rensselaer Polytechnic Institute.

Bartlmä, F. 1990 The propagation of detonation waves in channels of varying cross-section. *J. Fluid Mech.* **218**, 225–238.

Bdzil, J.B. & Short, M. 2017 Theory of Mach reflection of detonation at glancing incidence. *J. Fluid Mech.* **811**, 269–314.

Ben-Dor, G. 2007 *Shock Wave Reflection Phenomena*, 2nd edn. Springer-Verlag.

Ben-Dor, G., Dewey, J.M., McMillin, D.J. & Takayama, K. 1988 Experimental investigation of the asymptotically approached Mach reflection over the second surface in a double wedge reflection. *Exp. Fluids* **6**, 429–434.

Ben-Dor, G., Dewey, J.M. & Takayama, K. 1987 The reflection of a plane shock wave over a double wedge. *J. Fluid Mech.* **176**, 483–520.

Chen, D., Ma, H.H. & Wang, L.Q. 2023 Mach reflection of detonation wave on porous wall. *Phys. Fluids* **35**, 037109.

Desbordes, D. 1988 Transmission of overdriven plane detonations: critical diameter as a function of cell regularity and size. *Dyn. Explos.* **114**, 170–185.

EDL 2023 *SDToolbox: Numerical Tools for Shock and Detonation Wave Modeling*. GALCIT Report.California Institute of Technology. Available at: http://shepherd.caltech.edu/EDL/PublicResources/sdt/.

Edwards, D.H., Walker, J.R. & Nettleton, M.A. 1984 On the propagation of detonation waves along wedges. *Arch. Combust.* **4**, 197–209.

https://doi.org/10.1017/jfm.2026.11751 Published online by Cambridge University Press

FAY, J.A. 1959 Two-dimensional gaseous detonations: velocity deficit. *Phys. Fluids* **2**, 283–289.
FORTIN, Y., LIU, J. & LEE, J.H.S. 2015 Mach reflection of cellular detonations. *Combust. Flame* **162**, 819–824.
GAVRILENKO, T.P., NIKOLAEV, Y.A. & TOPCHIYAN, M.E. 1979 Supercompressed detonation waves. *Combust. Explos. Shock Waves* **15**, 659–662.
GAVRILENKO, T.P., NIKOLAEV, Y.A. & TOPCHIYAN, M.E. 1983 Overdriven gaseous detonations. *Prog. Astronaut. Aeronaut.* **87**, 244–250.
GOODWIN, D.G. 2003 An open-source, extensible software suite for CVD process simulation. In *Proceedings of CVD XVI and Euro CVD Fourteen* (ed. M. ALLENDORF), pp. 155–162. The Electrochemical Society, Inc.
GRAY, J.A.T., LEMKE, M., REISS, J., PASCHEREIT, J., SESTERHENN, C.O., & MOECK, J.P. 2017 A compact shock-focusing geometry for detonation initiation: experiments and adjoint-based variational data assimilation. *Combust. Flame* **183**, 144–156.
GUO, C., THOMAS, G., LI, J. & ZHANG, D. 2002 Experimental study of gaseous detonation propagation over acoustically absorbing walls. *Shock Waves* **11**, 353–359.
GUO, C., WANG, C., XU, S. & ZHANG, H. 2007 Cellular pattern evolution in gaseous detonation diffraction in a 90°-branched channel. *Combust. Flame* **148**, 89–99.
HANANA, M. & LEFEBVRE, M.H. 2001 Pressure profiles in detonation cells with rectangular and diagonal structures. *Shock Waves* **11**, 77–88.
HUANG, Z.W. & XU, B. 1987 Relation between cell size and detonation parameters in overdriven gaseous detonation. *Combust. Flame* **67**, 95–98.
JI, T., MA, H.H. & WANG, L.Q. 2023 Mach reflection of detonation waves over a porous concave wedge. *Phy. Fluids* **35**, 087114.
KANESHIGE, M. & SHEPHERD, J.E. 1997 *Detonation Database*. California Institute of Technology.
LEE, J.H.S. 1984 Dynamic parameters of gaseous detonations. *Annu. Rev. Fluid Mech.* **16**, 311–336.
LI, H. & BEN-DOR, G. 1998 A modified CCW theory for detonation waves. *Combust. Flame* **113**, 1–12.
LI, H. & BEN-DOR, G. 1999 Interaction of two Mach reflections on concave double wedges – analytical model. *Shock Waves* **9**, 259–268.
LI, H., BEN-DOR, G. & GRONIG, H. 1997 Analytical study of the oblique reflection of detonation waves. *AIAA J.* **35**, 1712–1720.
LI, J., JIANG, C., PAN, J.F., CHEN, W. & ZUO, L. 2025 Effects of frontal curvatures of a weak cellular detonation wave on its reflection over wedges with large angles. *Intl J. Hydrogen Energy* **193**, 152399.
LI, J., LAI, W.H., CHUNG, K. & LU, F.K. 2008 Experimental study on transmission of an overdriven detonation wave from propane/oxygen to propane/air. *Combust. Flame* **154**, 331–345.
LI, J. & LEE, J.H.S. 2016 Numerical simulation of Mach reflection of cellular detonations. *Shock Waves* **26**, 673–682.
LI, J., NING, J. & LEE, J.H.S. 2015 Mach reflection of a ZND detonation wave. *Shock Waves* **25**, 293–304.
LI, J., PAN, J.F., JIANG, C., SHI, X., ZHU, Y. & QUAYE, E.K. 2022 Numerical study on detonation reflections over concave and convex double wedges. *Intl J. Hydrogen Energy* **57**, 17033–17044.
LI, J., REN, H., WANG, X. & NING, J. 2018 Length scale effect on Mach reflection of cellular detonations. *Combust. Flame* **189**, 378–392.
MAZAHERI, K., MAHMOUDI, Y., SABZPOOSHANI, M. & RADULESCU, M.I. 2015 Experimental and numerical investigation of propagation mechanism of gaseous detonations in channels with porous walls. *Combust. Flame* **162**, 2638–2659.
MEAGHER, P.A., SHI, X., JAYARAMAN, A.S., KATERIS, K., ZHAO, X. & WANG, H. 2023 The hydrodynamic origin of the detonation cell. In *The 29th (2023) International Colloquium on the Dynamics of Explosions and Reactive Systems*. ICDERS.
MELTZER, J., SHEPHERD, J.E., AKBAR, R. & SABET, A. 1993 Mach reflection of detonation waves. *Prog. Astronaut. Aeronaut.* **153**, 78–78.
NG, H.D. 2005 The effect of chemical reaction kinetics on the structure of gaseous detonations. School PhD theies, McGill University.
NG, H.D. & ZHANG, F. 2011 Detonation instability. In *Shock Waves Science and Technology Library* (ed. F. Zhang), vol. 6, pp. 107–212. Springer Berlin, Heidelberg.
OHYAGI, S., OBARA, T., NAKATA, F. & HOSHI, S. 2000 A numerical simulation of reflection processes of a detonation wave on a wedge. *Shock Waves* **10**, 185–190.
ONG, R. 1955 On the interaction of a Chapman–Jouget detonation wave with a wedge. School PhD thesis, University of Michigan.
REN, H., JING, T. & LI, J. 2021 Study on cell size variation in overdriven gaseous detonations. *Acta Mech. Sin.* **37**, 938–953.

https://doi.org/10.1017/jfm.2026.11751 Published online by Cambridge University Press

SHEPHERD, J.E., SCHULTZ, E. & AKBAR, R. 1999 Detonation diffraction. In *22nd International Symposium on Shock Waves, Imperial College, London, UK*.

SOLOUKHIN, R.A. & RAGLAND, K.W. 1969 Ignition processes in expanding in gases. *Combust. Flame* **13**, 295–302.

SOW, A., SEMENKO, R.E. & KASIMOV, A.R. 2017 On a stabilization mechanism for low-velocity detonations. *J. Fluid Mech.* **816**, 539–553.

STREHLOW, R.A. 1969 The nature of transverse waves in detonations. *Astronaut. Acta* **14**, 539–548.

TAKAYAMA, K. & BEN-DOR, G. 1988 Application of streak camera photography for the study of shock wave reflections over a double wedge. *Exp. Fluids* **6**, 11–15.

TANG YUK, K.C., MI, X.C., LEE, J.H.S. & NG, H.D. 2018 Transmission of a detonation across a density interface. *Shock Waves* **28**, 967–979.

THOMAS, G.O. & WILLIAMS, R.L. 2002 Detonation interaction with wedges and bends. *Shock Waves* **11**, 481–492.

VON NEUMANN, J. 1963 *Collected Works*, vol. 6. Pergamon Press.

WANG, C.J., XU, S.L. & GUO, C.M. 2008 Gaseous detonation propagation in a bifurcated tube. *J. Fluid Mech.* **599**, 81–110.

WANG, L.Q. & MA, H.H. 2024 Detonation wave reflection over a concave–convex cylindrical wedge. *Shock Waves* **34**, 285–289.

WHITHAM, G.B. 1957 A new approach to problems of shock dynamics. Part 1. Two-dimensional problems. *J. Fluid Mech.* **2**, 145–171.

WOLAŃSKI, P. 2013 Detonative propulsion. *Proc. Combust. Inst.* **34**, 125–158.

XIAO, Q., SOW, A., MAXWELL, B.M. & RADULESCU, M.I. 2021 Effect of boundary layer losses on 2D detonation cellular structures. *Proc. Combust. Inst.* **38**, 3641–3649.

XIE, P., HAN, Z.Y. & TAKAYAMA, K. 2005 A study of the interaction between two triple points. *Shock Waves* **14**, 29–36.

ZHOU, Z.Y., MA, H.H. & WANG, L.Q. 2024 Mach reflection of detonation waves with velocity deficits. *Combust. Flame* **270**, 113754.

ZHOU, Z.Y., MA, H.H., WANG, L.Q. & YUAN, F. 2025 Detonation diffraction in divergent channels with smooth and porous walls. *AIAA J.* **63**, 4717–4725.

https://doi.org/10.1017/jfm.2026.11751 Published online by Cambridge University Press